Final Master's Thesis

Space and Aeronautical Engineering

Analysis of ionospheric scintillation in GNSS signals

Lorena Tortajada Ropero

Directors: Adrià Rovira, José Miguel Juan

Escola Superior d'Enginyeries Industrial, Aeroespacial i Audiovisual de Terrassa

Universitat Politècnica de Catalunya

Terrassa, June 22, 2021

Abstract

Scintillation is a particular type of space weather disturbance that currently limits the accuracy and availability of the Global Navigation Satellite System. The present final master's thesis aims to study the characteristics of satellite navigation techniques. First, evaluate the impact of scintillation on the frequencies and signals used in space-based navigation systems. For this, the TFM will make use of the Geodetic Detrending technique developed by research group Astronomy and Geomatics of the Universitat Politecnica de Catalunya (gAGE). The final objective of this TFM is to show that, once the scintillation effect has been detected, there are receptors that in combination with certain signals can influence navigation or the study of the atmosphere.

Resumen

El centelleo es un tipo particular de perturbación del clima espacial que actualmente limita la precisión y disponibilidad del Sistema Global de Navegación por Satélite. El presente trabajo de final de máster tiene como objetivo estudiar las características de las técnicas de navegación por satélite. Primero, evaluar el impacto del centelleo en las frecuencias y señales utilizadas en los sistemas de navegación basados en el espacio. Para ello, el TFM hará uso de la técnica Geodetic Detrending desarrollada por el grupo de investigación de Astronomía y Geomática de la Universitat Politecnica de Catalunya (gAGE). El objetivo final del presente TFM es mostrar que, una vez detectado el efecto de centelleo, existen receptores que en combinación con ciertas señales pueden influenciar a la navegación o el estudio de la atmósfera.

Contents

List of Figures

List of Tables

Chapter 1

Introduction

Global Navigation Satellite Systems (GNSS) includes a heterogeneous community of users equipped with more than 5 billion GNSS receivers, a number that is expected to grow to 8 milion by 2020 [11]. This GNSS' growth is related to an increasing number of GNSS satellite constellations. Two constellations have already declared their Full Operational Capability (FOC). One of them, the Global Positionins System (GPS, US AirForce) completed in 1994 and the other one completed in 1995: the Global Navigation Satellite System (GLONASS-Russian Federal Space Agency). Two additional constellations are being completed: the BeiDou Navigation Satellite System (BDS,China National Space Administration) and the Galileo (European Comission).

The four GNSS – GPS (USA), GLONASS (RU), BeiDou (PRC) and Galileo (EU) – will continue to provide navigation services with global coverage for the foreseeable future, with more than 100 GNSS satellites in Medium Earth Orbit (MEO) [20].

BeiDou-3 satellites have been launched during 2018-2019, and Galileo 'Batch 3' satellites are due to follow suit from 2021 to complete and maintain the constellation.

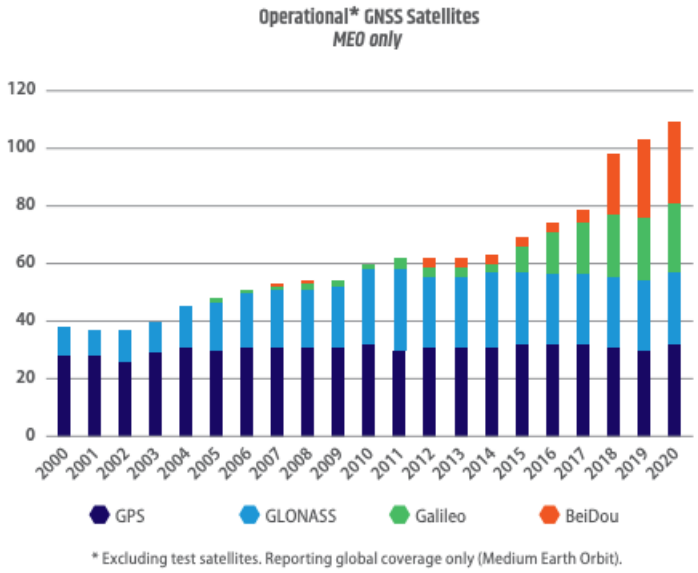

Figure 1.1: Operational GNSS Satellites in MEO from [20].

1.1 Motivation & Objectives

Furthermore, with the evoution of 5G in users, contrary to existing radio networks where positioning has only been an add-on feature, for 5G mobile radio networks the positioning is seen as an integral part of the system design and will play a key role, enabling a huge amount of different location-based services and applications. Thus, it is expected that hybrid GNSS/5G will be the core of future location engines for many applications in the Internet of Things (IoT) domain, with a significantly improved location performance in cities [20]. Also, the aviation community is affected by the improvements made by GNSS thecniques.

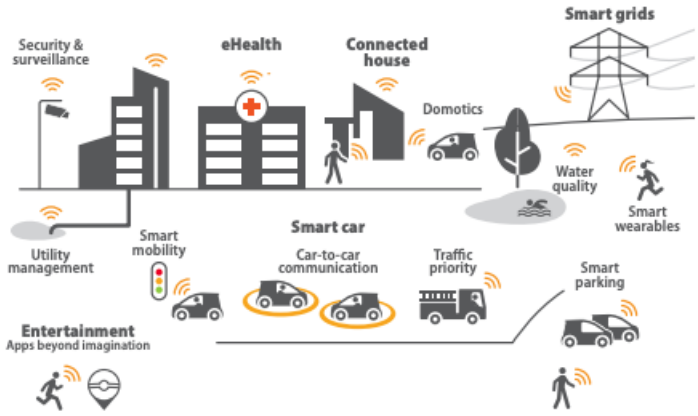

Figure 1.2: Examples of telecommunication applications profiting from 5G [20].

Thus, to meet the increase in GNSS-based services as well as its increasing accuracy of measurements, it is logical to analyze and mitigate those effects that affect the service the most. Specifically, the effect studied, as mentioned above, is the identification, mitigation and correction of effects in the ionosphere, an issue that is one of the current challeges for aerospace, aviation and ground-based operations including precise GNSS navigation [13].

The particular ionospheric perturbation that this project will cover is the scintillation introduced in 1960 (see for istance [4]). It is related to flunctiations in the electromagnetic signals when refracted and/or diffracted during their traver from the satellite to the receiver. Irregularities in the distribution of electrons affect the intensity and pashe of GNSS signals.

Up to present, most of researches for scintillation characterization has been developed with ionospheric scintillation monitoring receivers (ISMR). These receivers are capable of sampling the GNSS signal at a high rate. They need a very stable clock, so their cost is also high. ISMRs present some disadvantages. First, their high sampling-rate generates an enourmous constant amount of output data while scintillation only occurs at specific instants that we will see after.Because of the large storing capabilities that ISMRs require, their data are not tipically made available to the public. Second, the number of ISMRs is limited to few tens of receivers in the world. This facts limits scintiñlation studies to those few locations.

For those reasons, the following research aims to identify and characterize the impact of scintillation on the frequencies and signals used in space by navigation systems. Moreover, this project will use data from Geodetic Receivers. These second group of revceivers are multi-frequency, can support different constellations (multi-gnss) and also provide low noise measurements. They are part of the International GNSS Service (IGS) network. In addition, they are more extended by different earth locations than not ISRMs.

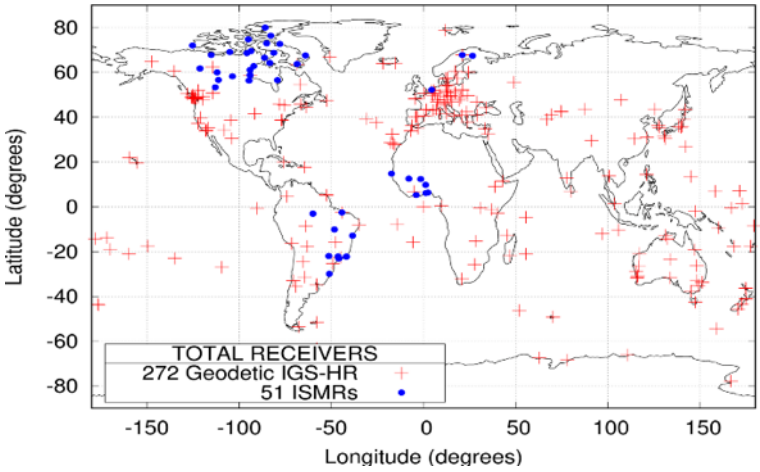

Figure 1.3: Distribution of ISMRs (blue circles) vs the geodetic-grade receivers (red pluses) types from [19].

To this end, the project will use the Geodetic Detrending (GD) technique developped by the research group of Astronomy and Geomatics (gAGE) introuduced by [12]. The final objective presented below is to show the correlation between scintillation effect and the loss of performance for high accuracy navitation or atmosphere study.

The structure of the work is presented. First, an introduction is made to determine the state of the art of the scintillation phenomenon in the ionosphere as well as its main indices that characterize it. Chapter 2 details the de-trending process applied to signals to obtain scintillation measurements that will lead to results. Chapter 3 presents the range of data to be observed and the reason for its selection. Chapter 4 selects from the dataset determined above, the two main days with scintillation. To do this, the scintillation detection thresholds of two of the indices presented in Chapter 3 are explained in the first stay, then the results divided into constellations and their conclusions are presented. In the fifth chapter, one more level is deepened, and the specific case of the two days chosen in the previous chapter will be studied. In Chapter 6, the analisis focusses on certain satellites and both results and conclusions obtained for certain satellites, stations and time intervals are presented. A final Chapter 7 of conclusions summarizes the most important ideas obtained from the study. Finally, the budget and social/environmental implications of the study are presented in Chapter 8 and 9 respectively.

Below are presented the basic concepts around which the study is carried out are introduced, that is, the ionosphere and more specifically, the scintillation phenomenon that occurs in it. Later, the indicators that are currently used to detect this phenomenon will be introduced. Finally, GD technique that will be used for frequency analysis will be presented due to its good performance.

1.2 The ionosphere

The ionosphere is that part of the terrestrial atmosphere that extends from about 60 km up to more than 2000 km. As its name implies, it contains a partially ionised medium, as a result of solar X- and Extreme UltraViolet (EUV) rays in the solar radiation and the incidence of charged particles [10].

The propagation speed of GNSS electromagnetic signals in the ionosphere depends on its electron density, which is typically driven by two main processes. During the day, the Sun's radiation ionises neutral atoms to produce free electrons and ions. During the night, the recombination process prevails, where free electrons are recombined with ions to produce neutral particles, which leads to a reduction in the electron density.

A medium where the angular frequency ω and the wave number k are not proportional is a dispersive medium (i.e. the wave propagation speed and hence the refractive index depend

on the frequency). This is the case with the ionosphere where ω and k are related, to a first approximation, by [2]:

$$w^2 = c^2k^2 + w_p^2 \tag{1.1}$$

where c is the propagation speed of a signal in a vacuum, $\omega_p = 2\pi \cdot fp$ with $fp = 8.98\sqrt{Ne}$ in Hz and Ne is the electron density (in e^-/m^3).

Equation (1.1) is called the relation of dispersion of the ionosphere, and ω_p is called the *critical frequency* of the ionospheric plasma, in the sense that signals with $\omega \leq \omega_p$ will be reflected and signals with $\omega > \omega_p$ will pass through the plasma. This is the case for GNSS signals whose frequencies are of the order of 1 GHz.

Following the calculations in [10] about the refractive index of ionosphere, substituting the phase and group refractive indices it can be seen that phase measurements are advanced on crossing the ionosphere, that is a negative delay, while the code measurements undergo a positive delay:

$$\Delta_{ionoph,f} = -\frac{40.3}{f^2}\int Ne\, dl \tag{1.2}$$

$$\Delta_{ionogr,f} = +\frac{40.3}{f^2}\int Ne\, dl \tag{1.3}$$

The differences $\Delta_{ionoph,f}$ and $\Delta_{ionogr,f}$ are called the phase and code ionospheric refraction, respectively, and the integral is defined as the Slant TEC (STEC):

$$STEC = \int Ne\, dl \tag{1.4}$$

Usually, the STEC is given in TEC units (TECUs), where 1 TECU = 10^{16} e^-/m^2 and the ionospheric delay I_f (at the frequency f) is written as:

$$I_f = \Delta_{ionogr,f} = \alpha_f STEC \tag{1.5}$$

with

$$\alpha_f = \frac{40.3 \cdot 10^{16}}{f^2} m_{signal_{delay}}/TECU \tag{1.6}$$

The electron density in the ionosphere changes with height, having a maximum of $Ne \approx 10^{11}$ to 10^{12} e^-/m^3 around 300-500 km. The TEC, and hence the ionospheric refraction, depend on the geographic location of the receiver, the hour of day and the intensity of the solar activity.

As the ionosphere is a dispersive medium, refraction of the GNSS signals depends on their frequencies (as the squared inverse). This dependence on the signal frequency allows us to remove its effect by up to more than 99.9% using two-frequency measurements, which allows to build the so-called ionosphere free combination of carrier phases (IF). However, single-frequency receivers have to apply an ionospheric prediction model to remove this effect.

As commented previously, equation (1.1) is a simplification of the relation of dispersion of the ionosphere, where the dependence of the refractive index on the magnetic field **B** has been neglected. If such terms are taken into account, higher order ionospheric terms appear (but they represent less than 0.1% of the total effect). Therefore, in this case study, we will work with only first-order ionospheric effects.

As it can be seen in the following image, errors in ionosphere cannot be neglected and they have to be mitigated during the de-trending. GD technique does it.

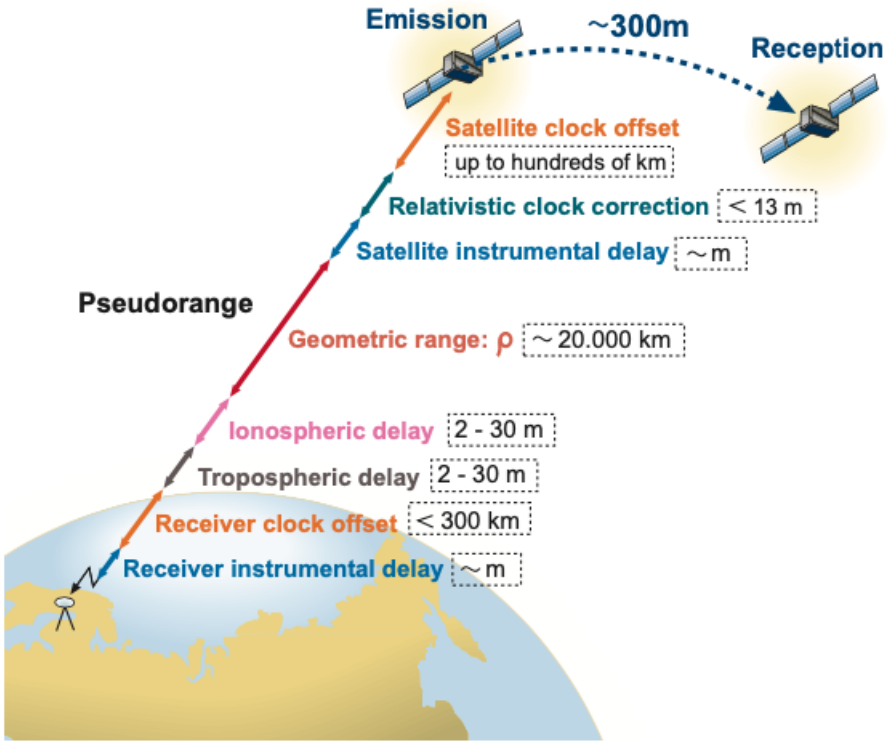

Figure 1.4: Possible measurements errors during location from [3]

Until now, we have talked about the refractive part of the ionosphere. However, as indicated in [18], the ionospheric effect I_f can be decomposed into two different terms: $I_f = I_f^r + I_f^d$, where:

- I_f^r is the refractive ionospheric effect at frequency f, which can be eliminated up to 99.9% with the dual-frequency ionosphere-free (IF) combination.
- I_f^d is the diffractive ionospheric effect at frequency f. In low-latitude regions, ionospheric irregularities with a size close to the Fresnel length for GNSS frequencies, which is 400 m, can scatter the signal into multiple paths producing signal diffraction. The diffractive

effects can be observed as rapid fluctuations in both carrier-phase and signal amplitude, losses of lock, and frequent cycle-slips. Unlike the ionospheric refraction, the diffraction is not proportional to the inverse squared frequency. Thus, diffractive effects cannot be eliminated with the IF combination and here it is where the concept of scintillation comes up.

1.3 The scintillation effect

Ionospheric scintillation occurs when signals experience fast fluctuations, when they are diffracted by irregularities of the electron distribution along their propagation paths, disrupting the performance of space-based communication and navigation systems. Scintillation causes the GNSS signals to have an increased level of noise or even experience a loss of lock on the receiver tracking. For that reason, scintillation has become one of the major concerns in navigation.

According to [18], these irregularities are present at equatorial and high latitudes, predominantly in the F layer at altitudes comprised from 250 to 400 km, but also in the E layer at high latitudes with altitudes ranging from 90 to 120 km. Ionospheric perturbations affecting GNSS are associated with space weather events (such as geomagnetic storms) at high latitudes, and associated with plasma bubbles after the sunset at low latitudes [15]. This phenomenon endangers GNSS navigation by giving rise to significant fluctuations in the amplitude and/or the carrier-phase of GNSS measurements, or causing losses of lock in the tracking loop of the GNSS receiver.

From previous studies [15], it is possible to state that the occurrence of ionospheric scintillation and its intensity are strongly dependent on latitude, local time, season of the year, solar cycle, and magnetic activity, presenting a strong degree of day to day variability.

Although scintillation may be a global phenomenon, the occurrence of scintillation is generally clustered around the geomagnetic equator ($\phi_{magnetic} \leq |25|^{\circ}$) and in both polar $\phi_{magnetic} > |60|^{\circ}$). In the particular case of high latitudes, scintillation appears to be associated with geomagnetic storms or solar events, whereas in equatorial latitudes, it is associated with plasma movements that typically occur after the local sunset.

Concerning the size of the irregularities in the electron distribution, these irregularities can range from metres to tens of kilometres, and their drift velocities (in combination with the scan velocity of the GNSS) can span from tens to hundreds of metres per second, in low latitudes, up to some kilometres per second, in high latitudes. GNSS signals experience rapid phase variations, which can be tracked by ISMRs. However, in this study, measurements will be carried out with geodetic receivers, which are open loop receivers, as expressed in the previous chapter.

1.4 Scintillation indicators

Several indices have been developed to measure the effect of scintillation activity on GNSS signals:

1. **The amplitude scintillation index,** S_4, is defined as the standard deviation of the signal power normalized by its mean [1]:

$$S_4 = \sqrt{\frac{< SI^2 > - < SI >^2}{< SI >^2}} \tag{1.7}$$

where SI denotes the signal intensity. S_4 is typically computed over a period of one minute, and its values typically range from 0 to 1 (although it may be greater than 1).

2. **The phase scintillation index,** σ_φ is defined as the standard deviation of the de-trended carrier phase:

$$\sigma_\varphi = \sqrt{< \varphi^2 > - < \varphi >^2} \tag{1.8}$$

where φ denotes the de-trended carrier phase measurement. This standard deviation is calculated over a certain time period, typically one minute, and accounts for carrier phase fluctuations. The computation of σ_φ takes advantage of the high-frequency nature of the carrier phase fluctuations associated with scintillation. In this sense, the isolation of the scintillation effect on the carrier phase is performed by filtering the carrier phase, typically with a 6th order high-pass Butterworth filter [7]. Thus, all the fluctuations introduced by other effects (such as geometry and tropospheric delay) that usually occur at lower frequencies are removed. However, other high-frequency effects that could be present on the carrier phase data, such as the receiver clock errors or cycle-slips, may distort the calculation of the σ_φ index. Moreover, the particular characteristics of the filter can have an influence on the σ_φ retrievals [9].

3. **The rate of change of the total electron content index (ROTI)** defined in [5] is an example of a scintillation indicator that can be computed from dual-frequency measurements at low frequency (typically 1/30 Hz). The ROTI is defined as the standard deviation of the time derivative of the ionospheric delay, i.e. TEC. The slant TEC (STEC) is measured directly from the geometric-free combination of the carrier phase measurements (L_{GF} = L1 - L2), where the hardware biases and ambiguities of the carrier phases are removed in the derivation:

$$ROTI = \sqrt{< (\frac{\Delta L_{GF}}{\Delta t}^2) > - (\frac{\Delta L_{GF}}{\Delta t})^2} \tag{1.9}$$

This standard deviation is computed over a time window of pre-defined length, which depends on the sampling rate (typically 5 min with 1/30 Hz data or 1 min with 1 Hz

data). In fact, ROTI determinations are influenced by the selected sampling rate and time interval for the calculation. In addition, a key element in the ROTI computation is the correct identification of the satellite arcs (i.e, continuous carrier-phase measurements without cycle slip), which depends on the receiver processing algorithms.

4. **The ROTIM**: Defined by the following equation

$$ROTIM = \sigma_\tau(\frac{\dot{L_{GF}}}{M(\epsilon)}) \tag{1.10}$$

where σ_τ denotes the standard deviation computed with a moving window of length $\tau = 10$ s using sample rate of 1 Hz and L_{GF}= L1-L2. The only difference of ROTIM with respect to ROTI is that, in order to mitigate large ROTI values at low elevations, it is applied to all $\dot{L_{GF}}$ observations a mapping function $M(\epsilon)$, that depends on the satellite elevation ϵ:

$$M(\epsilon) = \sqrt{1 - (\frac{R_E}{R_E + h} cos(\epsilon))^2} \tag{1.11}$$

where R_E is the radius of the Earth and h is the height of the ionospheric layer (assumed at 350 km).

5. **The IF-sigma indicator**: After the cycle-slips in GNSS tracking are identified and corrected, the navigation solution is only affected by the remaining residual of the L_{IF}, the diffractive part, which, unlike the refractive part, remains under scintillation. In this sense, the standard deviation of such residuals can be used as a parameter to reflect the degradation in the navigation that any receiver would experience, provided the phase jumps are detected and fixed. Such standard deviation is defined as IF-sigma,computed over a sliding window of 1 minute. The observed increase in the value of σ_{IF} corresponds to the hours associated with the presence of scintillations (observed as rapid fluctuations in the residuals of the L_{IF} combination).

6. **The AATR index [15]**: Once the arcs of signal tracking at receivers are correctly identified, the variation of the STEC between two consecutive observations separated Δt, can be computed for a given epoch, t, as:

$$\Delta STEC_i^j(t) = {L_{GF}}_i^j(t) - {L_{GF}}_i^j(t - \Delta t) \tag{1.12}$$

where i denotes the receiver and j the satellite. Because we are interested in the rate of the STEC variation, we compute the instantaneous AATR:

$$AATR_i^j(t) = \frac{1}{M(\epsilon)^2} \frac{\Delta STEC_i^j(t)}{\Delta t} \tag{1.13}$$

where Δt is the sampling rate of the carrier-phase measurements (typically 1/30 Hz) and $M(\epsilon)$ is an obliquity, or slant, factor defined as the secant of the zenith angle at the mean

ionospheric height, that is typically assumed at a 350 km of altitude. $M(\epsilon)$ projects the vertical to slant delay in a thin-shell model of the ionosphere and only depends on the satellite elevation (ϵ). The purpose of dividing by the mapping function is to compare observations sampled at different elevations. The square of the mapping factor mitigates large AATR values at low elevations and, conversely, it assigns a large weight to high-elevation observations where the thin layer model is expected to be more accurate.

Finally, the RMS of the instantaneous AATR, is computed for a pre-defined period for all "j" satellites in view from a particular station, resulting into the AATR index per a given "i" receiver as:

$$RMS_{AATR,i}(T) = \sqrt{\frac{1}{N}\sum_{t=T}^{T+\Delta T}\sum_{j=i}^{n_{sat}(t)}(ATTR_i^j(t))^2} \tag{1.14}$$

where N is total number of observations during the selected interval Δt (typically one hour), after having summed all satellites in view, nsat(t), at every epoch t.

1.4.1 AATR vs ROTI index

There are also some differences between AATR and ROTI index [15]. The main differences of the AATR index with respect to the ROTI are summarised as follows. The temporal resolution of the AATR is lower than the ROTI; Both AATR and ROTI are computed every five minutes. The number of satellites involved in the AATR is greater than in the ROTI; AATR uses the rates of all the satellites in view, whereas the ROTI is computed on a satellite-per-satellite basis. In consequence, the AATR index sounds a wider area than each individual satellite track, with a considerable less amount of output than the ROTI. This sounding can only be roughly achieved averaging values of ROTI for different receivers, for instance to generate ROTI maps in longitude/latitude grids or magnetic local time.

1.4.2 σ_{IF} vs S_4 and ROTI index

σ_{IF} accounts for essentially the same diffractive effect on the GNSS signal as S_4 does. Moreover, σ_{IF} is computed from the L_{IF} , its value relates the degradation of precise navigation with the scintillation [12].

On the one hand, because ROTI is based on the geometry-free combination, it does not distinguish diffractive effects (large S_4 and σ_{IF} values) from refractive effects (moderate S_4 and σ_{IF} values). On the other hand, if the cycle-slips associated with scintillation are not corrected, then the ROTI value will be overestimated, being large values of ROTI linked to the receiver internal software processes rather than to actual ionospheric activity.

Chapter 2

Methodology

2.1 Geodetic detrending

The carrier-phase measurement is

$$L_f = \rho + \delta_{ant} + \delta_{tide} + \delta t_{rec} - \delta t^{sat} + Tr + I_f + (B_f + \lambda_f N_f) + w_f + \epsilon_f \tag{2.1}$$

where the frequency-independent terms are: the geometric range ρ between the satellite antenna phase centre (APC) at emission time and the receiver APC at reception time, the effect δ_{ant} caused by phase centre variations of the satellite and the receiver, the solid tides effect δ_{tide}, the receiver and satellite clock offsets, δt_{rec} and δt^{sat}, and the tropospheric delay Tr.

Frequency-dependent terms at frequency f are: the phase ambiguity including a real-valued offset B_f and an integer number N_f of cycles bias with wavelength λ_f, the phase wind-up effect w_f, ϵ_f is the effect of noise and multipath error in carrier-phase measurements. The ionospheric effect I_f is divided into two different terms: $I_f^r + I_f^d$.

The first step is to apply the geodetic detrending that consists in subtracting from the carrier-phase L_f in Eq. 2.1 the terms that can be estimated with well-known geodetic models -as Precise Point Positining (PPP) [6]- such as δ_{tide}, w_f and T_r and using IGS products such as δ_{ant} and δt^{sat}. The geometric range ρ can be computed with few centimetres of accuracy with the precisely known coordinates of the APC of the station and the satellite thanks to the antenna exchange format (ANTEX) file provided by IGS. Hence, it is obtained the residual $\hat{r}_{Lf}$ to each frequency measurement:

$$\hat{r}_{Lf} = \delta t_{rec} + (B_f + \lambda_f N_f) + I_f^r + I_f^d + \epsilon_f \tag{2.2}$$

[18] compares the phase scintillation index σ_φ for three different sources:

- $\sigma_{\varphi f}$ at 50 Hz: Output of ISMRs calculated as Eq. 1.8 from data with sample rate of 50Hz. This can be considered the reference value;

- $\sigma_{\widehat{\theta}}$ at 1 Hz: Index calculated by using a conventional sixth-order Butterworth high pass filter HPF with carrier-phase measurements from a convential receiver, calculated from RINEX data with sample rate at 1 Hz.

- $\sigma_{\theta f}$ at 1 Hz: Index calculated using a proposed methodology in which the RX clock offset has been estimated from a conventional receiver, calculated from RINEX data with sample rate at 1 Hz.

The conclusions show that the proposed method overcomes some of the problems associated with ionospheric indicators. For instance, it is capable of estimating ionospheric fluctuations on each individual frequency rather than in a combination of signals, as occur with ROTI. This turns very adequate when studying diffractive scintillation at low latitude, in which effects are not proportional between frequencies. Furthermore, the accurate modelling of the carrier-phase measurements used allows identifying and correcting cycle-slips which are due to receiver artefacts. The results of the phase scintillation index $\sigma_{\theta f}$, obtained with the method, agree with the $\sigma_{\varphi f}$ provided by ISMRs at different frequencies.

Due to the advantages presented above, this project will follow the approach used by [18], the proposed geodetic de-trending method used will be detailed below.

The diagram of 2.1 presents the different modules explained hereafter. The first processing step is to model the carrier-phase measurements L_f to obtain the carrier-phase residuals $\dot{r}_{Lf}$. Then, the receiver-clock fluctuation is estimated $\hat{\delta}t_{rec}$ and removed, obtaining a clock-free carried phase residual r^*_{Lf}. The stability of the clock-corrected carrier-phases allows the identification and correction of the cycle-slips, producing a continuous residual r_{Lf} in real time. Finally, the strategy uses a HPF to obtain the high-frequency component θ_f of the carrier-phase residual that allows computing the phase scintillations index $\sigma_{\theta f}$ by means of a standard deviation over a moving window of 60 s.

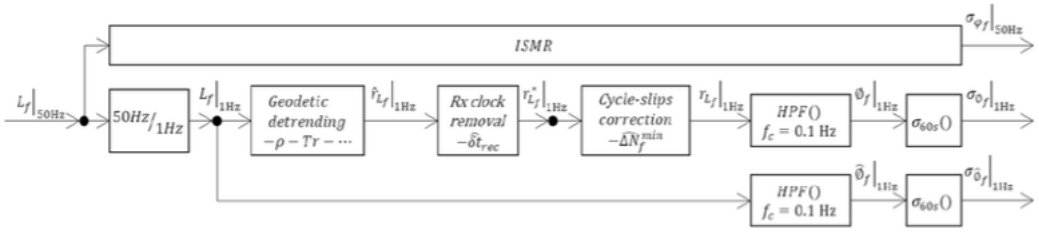

Figure 2.1: Methodology scheme for geodetic detrending from [18]

2.2 Receiver-clock estimation

The second step of the method consists in the determination of the fluctuation of the receiver clock δt_{rec} . In order to eliminate the 99.9% of the refractive ionospheric effect from $\hat{r}_{Lf1}$ and $\hat{r}_{Lf2}$, the IF combination of these residuals at frequencies f1 and f2 is built as follows:

$$\hat{r}_{L_{IF}} = \frac{f_1^2 \hat{r}_{Lf1} - f_2^2 \hat{r}_{Lf2}}{f_1^2 - f_2^2} = \delta t_{rec} + B_{IF} + \lambda_1^{IF} N_1 + \lambda_2^{IF} N_2 + I_{IF}^d + \epsilon_{IF} \tag{2.3}$$

As the result of the IF combination, one cycle slip in L1 causes an increase in $\hat{r}_{L_{IF}}$ of $\lambda_1^{IF} = \frac{f_1^2 \lambda_1}{f_1^2 - f_2^2} = 48.4cm$, and one cycle-slip in L2 causes an increase of $\lambda_2^{IF} = \frac{f_2^2 \lambda_2}{f_1^2 - f_2^2} = 37.7cm$.

From the mathematical point of view, and neglecting the noise term, the time derivative of $\hat{r}_{Lf1}$ of each satellite at epoch k can be computed, as follows:

$$\dot{\hat{r}}_{L_{IF}} = \frac{\hat{r}_{Lf1}(k) - \hat{r}_{Lf1}(k-1)}{t(k) - t(k-1)} = \delta \dot{t}_{rec} + \lambda_1^{IF} \Delta N_1 + \lambda_2^{IF} \Delta N_2 + \dot{I}_{IF}^d \tag{2.4}$$

where $\Delta N_1(k)$ $\Delta N_2(k)$ are, respectively, the numbers of cycles increasing in L1 and L2 when a cycle-slip occurs, the constant offset B_{IF} is cancelled out by the derivation, and the variation of diffractive ionospheric effect $\dot{I}_{IF}^d(k)$ is significant only during periods of diffractive scintillation. Therefore, $\hat{r}_{L_{IF}}$ with neither scintillation (i.e $\dot{I}_{IF}^d = 0$ nor cycle-slips (i.e $\Delta N_1 = \Delta N_2 = 0$) for all satellites will exhibit a common variation corresponding to the variation of the receiver clock $\dot{t}_{rec}$. Hence, one can estimate $\dot{\delta} t_{rec}$ by taking the mean value of $\dot{\hat{r}}_{L_{IF}}$ over all the satellites in view. In order to improve the estimation it is down-weighted those $\dot{\hat{r}}_{L_{IF}}$ values from satellites contaminated by cycle-slips and/or scintillation. In particular, ROTIM is used with an elevation mask of 5°. In contrast, when comparing the results with those of the phase scintillation index output by the ISMRs, a mask of 25° is used instead.

Therefore, ROTIM-weighted average of $\dot{\hat{r}}_{L_{IF}}$ from all satellites in view is used to estimate the time derivative of the receiver-clock offset, $\dot{\delta} t_{rec}$, according to the following expression:

$$\dot{\hat{\delta}} t_{rec} = \frac{\sum_{S=1}^{n} \cdot \frac{\dot{\hat{r}}_{L_{IF_s}}}{ROTIM_s^2}}{\sum_{S=1}^{n} \cdot \frac{1}{ROTIM_s^2}} \tag{2.5}$$

where n is the number of satellites in view, s is the index of each satellite, and $\dot{\hat{r}}_{L_{IF_s}}$ is the time derivative of 2.4 for satellie s. Thus, the fluctuation of the receiver-clock offset $\dot{\delta} t_{rec}$ is estimated as the numerical integral of $\dot{\hat{\delta}} t_{rec}$:

$$\hat{\delta} t_{rec} = \int_0^k \dot{\hat{\delta}} t_{rec}(n)\, dn \tag{2.6}$$

where k is the epoch of interest in which the receiver-clock $\hat{\delta} t_{rec}$ is to be evaluated, n indicates the integration variable between 0 and k, and dn is the integration step.

After removing the estimated receiver-clock fluctuation $\hat{\delta}t_{rec}$ from $\hat{r}_{L_{IF}}$ in 2.3, the residual r^*_{Lf} is obtained as:

$$r^*_{L_{IF}} = \hat{r}_{L_{IF}} - \hat{\delta}t_{rec}(k) = \dot{I}^d_{IF} + B_{IF} + \lambda_1^{IF} N_1 + \lambda_2^{IF} N_2 \tag{2.7}$$

This receiver-clock-free residual contains only the diffractive scintillation $\dot{I}^d_{IF}$, the integer ambiguities (N_1,N_2) and the constant ambiguity B_{IF}.

Finally,

$$r^*_{Lf} = \hat{r}_{Lf} - \hat{\delta}t_{rec} = (B_f + \lambda_f N_f) + I^r_f + I^d_f \tag{2.8}$$

2.3 Cycle-slips detector-corrector

The third step of the proposed method is to detect and correct cycle-slips occurring in the GNSS carrier-phase measurements. Cycle-slips are variations of integers, ΔN_f, that cause unalignment in r^*_{Lf} and therefore in $r^*_{L_{IF}}$ in the form of jumps. Those discontinuities are proportional to the wavelength λ_f^{IF} or λ_f,several times greater than the fluctuation attributable to the diffractive scintillation. Indeed, I^d_{IF} is typically less than 20 cm and during conditions of strong phase scintillation to 1 rad, which corresponds to 3 cm. Thus, cycle-slips can be isolated from scintillation. Conversely, undetected cycle-slips would contaminate the scintillation measurements. The cycle-slip detection–correction approach is described hereafter.

2.3.1 Cycle-slip detection

The cycle-slip occurrence is detected in the IF combination, exploiting the fact that the detrended $r^*_{L_{IF}}$ should be flat. A predicted value of $r^*_{L_{IF}}$ at epoch k, denoted as $\overline{r}_{L_{IF}}(k)$, is computed averaging the previous $r^*_{L_{IF}}$ during an interval of 6 s. When the difference between the actual value and the prediction, defined as $\xi_{IF} = r^*_{L_{IF}}(k) - \overline{r}_{L_{IF}}(k)$, is greater than a threshold $\theta_{IF} = 20cm$, a cycle-slip is detected.

2.3.2 Cycle-slip identification

Following the detection of one cycle-slip, it is targeted to identify on which frequency (or frequencies) the variation of cycles ΔN_1, and/or ΔN_2 occurred. If the computation is conclusive, the cycle-slip can be corrected and the uncombined signal r^*_{Lf} repaired. Otherwise, a new computation arc starts.

An initial estimation of the variation of the number of cycles from epoch t(k-1) to epoch t(k) is denoted as ΔN^0_f and can be computed subtracting the uncombined signal r^*_{Lf} between

adjacent epochs:

$$\Delta N_f^0(k) = \frac{r_{Lf}^*(k) - r_{Lf}^*(k-1)}{\lambda_f} \tag{2.9}$$

where it is assumed that ionospheric effects and constant ambiguity Bf do not vary in one second.

A search space is built within ±4 cycles from the rough initial estimation ΔN_f^0. That is, they look for nine possible integer values, denoted as $\widehat{\Delta N}_f^i$, for each frequency:

$$\Delta N_f^0 - 4 \leq \widehat{\Delta N}_f^i \leq \Delta N_f^0 + 4 \tag{2.10}$$

where index "i" denotes the "ith" integer candidate per frequency and ranges from $\widehat{\Delta N}_f^0$ to $\widehat{\Delta N}_f^9$. As there are two frequencies, the complete search space accounts for a total of 81 possible pairs being "i" and "j" the indices for candidates at frequencies f1 and f2, respectively.

For every "i, j" pair, they compute the residual at epoch k substracting the candidate integer values $\widehat{\Delta N}_1^i(k)$ and $\widehat{\Delta N}_2^j(k)$ to the combined $r_{L_{IF}}^*$:

$$r_{L_{IF}}^{i,j} = r_{L_{IF}}^*(k) - \lambda_1^{IF}\widehat{\Delta N}_1^i(k) - \lambda_2^{IF}\widehat{\Delta N}_2^j(k) = I_{IF}^d + B_{IF} \tag{2.11}$$

obtaining 81 candidate carrier-phase residuals, free of receiver clock and cycle-slips. It is selected the "i,j" pair that provides the minimum jump with respect to the previous six $r_{L_{IF}}^*$ samples,i.e. before the cycle-slip was detected.For this purpose, they use the predicted $\overline{r}_{L_{IF}}(k)$ in the "i, j" integer search with the following criteria:

- $r_{L_{IF}}^{i,j} - \overline{r}_{L_{IF}}(k)$ is minimized
- $r_{L_{IF}}^{i,j} - \overline{r}_{L_{IF}}(k) \leq \theta_{IF}$

The last condition guarantees that the selected pair ($\widehat{\Delta N}_1^{min}$, $\widehat{\Delta N}_2^{min}$) aligns with the previous samples within the cycle-slip tolerance previously defined. This protection is necessary, as they only evaluate ±4 cycles from the rough initial estimation,whereas the number of integers occurred by the cycle-slip, might fall out of the search space. In case that a cycle-slip is detected, but no candidate pair fulfils simultaneously the previous two conditions, the identification is inconclusive. Then, a new computing arc is started with the new value of N_f.

2.3.3 Cycle-slip correction

In case ΔN_1 and ΔN_2 are identified, the carrier-phase measurements of L1 and L2 are corrected by adding $\widehat{\Delta N}_f^{min}$ to the corresponding $r_{L_{IF}}^*$, r_{Lf}^* and the computation of the arc is continued:

$$r_{L_{IF}} = r^*_{L_{IF}} - \lambda_1^{IF}\widehat{\Delta N}_1^{min} - \lambda_2^{IF}\widehat{\Delta N}_2^{min} = I^d_{IF} + B_{IF} \tag{2.12}$$

and

$$r_{L_f} = r^*_{L_f} - \lambda_f\widehat{\Delta N}_f^{min} = I^r_f + I^d_f + B_f \tag{2.13}$$

where r_{L_f} contains the fluctuation of the carrier-phase attributable to refractive and diffractive ionospheric scintillation, whereas $r_{L_{IF}}$ contains only the diffractive one.

2.4 Phase scintillation index

The fourth and final step is to calculate the phase scintillation index. For this purpose, it is applied the aforementioned sixth-order Butterworth HPF with a cut-off frequency of 0.1 Hz to $r_{L_{IF}}$, obtaining its high-frequency component φ_f. If the GD has been done, only the HPF is needed, since the phase variations would only be due to the ionosphere. Then, the phase scintillation index is computed as the standard deviation of φ_f, using a windows of 60 s:

$$\sigma_\varphi = \sqrt{< \varphi_f^2 > - < \varphi_f >^2} \tag{2.14}$$

This procedure can be also applied to any frequency. The difference, as can be seen in (2.13), is that there would also be a refractive component.

Chapter 3

Data set evaluated

In order to analyze, characterize and obtain the behavior of the scintillation phenomenon present in GNSS signals, the first 120 days of 2020 have been analyzed. This analysis has been made from the data collected by stations located at different latitudes and distributed along the world map. This fact means that scintillation can be characterized in its different facets according to latitude, atmospheric phenomena and space wether, as introduced in the previous chapters.

This analysis is performed for the three GNSS constellations: GPS, Galileo, and GLONASS. Futhermore, the stations involved are represented in Fig 3.1, each station identified by four characters.

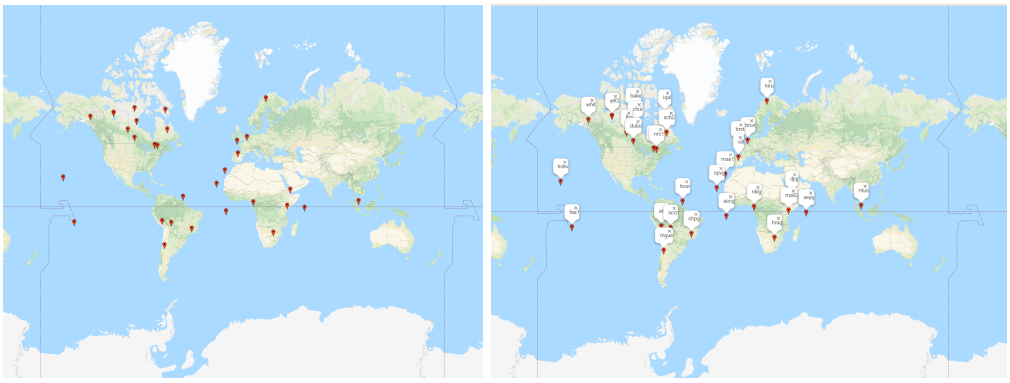

Figure 3.1: Stations locations and identifiers.

As it can be seen in Fig.3.1 the stations are spread all over the world.The following table shows the location of each station according to its longitude and latitude.

Name	Longitude (°)	Latitude (°)
algo	-78.071371356	45.763469076
areg	-71.492903655	-16.361150549
ascg	-14.332664658	-7.863951444
bake	-96.002350821	64.167195523
brux	4.358566764	50.609446439
chpg	-45.002375885	-22.545679630
chur	-94.088732732	58.588158087
djig	42.847066846	11.451180924
dubo	-95.866184324	50.069509348
faa1	-149.614307928	-17.444938964
flin	-101.978038254	54.543948097
iqal	-68.510501575	63.603018639
kiru	20.968453294	67.722681856
kour	-52.805960241	5.217217405
mal2	40.194146385	-2.976032414
mas1	-15.633273152	27.605416128
mgue	-69.397928477	-35.595050192
nklg	9.672128019	0.351540039
seyg	55.530632413	-4.647547177
vill	-3.951975873	40.253721369
yell	-114.480706591	62.322895091
yel2	-114.480849254	62.323324699
hrag	27.685181385	-25.739570044
kokv	-159.664937141	21.992336919
sch2	-66.832620361	54.650698572
nrc1	-75.623831174	45.261756205
scrz	-63.159674012	-17.685106168
brst	-4.496591142	48.189337212
whit	-135.222115293	60.586192300

Table 3.1: Stations locations

This project is focused on the specific case of GPS, were satellites transmit spread spectrum signals on L1 and L2 at 1575.42 and 1227.6 MHz, respectively.

GPS satellites can be identified by Pseudorandom Noise (PRN) codes. These codes are an important element of code division multiple access (CDMA) based GPS satellite navigation systems. Each satellite within a GNSS constellation has a unique PRN code that it transmits as part of the Coarse/Acquisition (C/A) navigation message. This code allows any receiver to identify exactly which satellite(s) it is receiving. Furthermore, GPS satellites are grouped into blocks based on the time they were launched and the features they contain. Older satellites belong to initial blocks and only contain the L1 and L2W signal. Starting with the IIR-M block, the satellites include a new military signal and a more robust civilian signal, known as L2C.

The following tables show the GPS satellites available for the first 120 days of 2020, the signals they use, their PRN and the block to which they belong.

PRN	SV	Block Type	SAT	Launch Date (UTC)	Positioning Signals
13	43	IIR	GPS 2R-2	1997/7/23	L1C/A,L2W
20	51	IIR	GPS 2R-4	2000/5/11	L1C/A,L2W
28	44	IIR	GPS 2R-5	2000/7/16	L1C/A,L2W
16	56	IIR	GPS 2R-8	2003/1/29	L1C/A,L2W
21	45	IIR	GPS 2R-9	2003/3/31	L1C/A,L2W
22	47	IIR	GPS 2R-10	2003/12/21	L1C/A,L2W
19	59	IIR	GPS 2R-11	2004/3/20	L1C/A,L2W
2	61	IIR	GPS 2R-13	2004/11/6	L1C/A,L2W
17	53	IIR-M	GPS 2R-14M	2005/9/26	L1C/A,L2C,L2W
31	52	IIR-M	GPS 2R-15M	2006/9/25	L1C/A,L2C,L2W
12	58	IIR-M	GPS 2R-16M	2006/11/17	L1C/A,L2C,L2W
15	55	IIR-M	GPS 2R-17M	2007/10/17	L1C/A,L2C,L2W
29	57	IIR-M	GPS 2R-18M	2007/12/20	L1C/A,L2C,L2W
7	48	IIR-M	GPS 2R-19M	2008/3/15	L1C/A,L2C,L2W
5	50	IIR-M	GPS 2R-21M	2009/8/17	L1C/A,L2C,L2W
25	62	IIF	GPS 2F-1	2010/5/28	L1C/A,L2C,L2W,L5
1	63	IIF	GPS 2F-2	2011/7/16	L1C/A,L2C,L2W,L5
24	65	IIF	GPS 2F-3	2012/10/4	L1C/A,L2C,L2W,L5
27	66	IIF	GPS 2F-4	2013/5/15	L1C/A,L2C,L2W,L5
30	64	IIF	GPS 2F-5	2014/2/21	L1C/A,L2C,L2W,L5
6	67	IIF	GPS 2F-6	2014/5/17	L1C/A,L2C,L2W,L5
9	68	IIF	GPS 2F-7	2014/8/2	L1C/A,L2C,L2W,L5
3	69	IIF	GPS 2F-8	2014/10/29	L1C/A,L2C,L2W,L5
26	71	IIF	GPS 2F-9	2015/3/25	L1C/A,L2C,L2W,L5
8	72	IIF	GPS 2F-10	2015/7/15	L1C/A,L2C,L2W,L5
10	73	IIF	GPS 2F-11	2015/10/31	L1C/A,L2C,L2W,L5
32	70	IIF	GPS 2F-12	2016/2/5	L1C/A,L2C,L2W,L5
4	74	III	GPS 3-1	2018/12/23	L1C/A,L2C,L2W,L5
18	75	III	GPS 3-2	2019/8/22	L1C/A,L2C,L2W,L5

Table 3.2: GPS available satellites in the first 120 days of 2020 from [23]

It should be noted that among 29 GPS total satellites, 14 have L5/L2C and 7 have only L2C, but instead there are 8 satellites with only L2W.

Throughout the project, the aim will be to obtain those days among the first 120 of 2020 that suffer most from the scintillation phenomenon, as well as to identify in which stations it has a greater incidence. Once the days and stations have been obtained, the satellites of them are analyzed to select those satellites with the highest scintillation values. For these satellites, the GPS L1 and L2 signals as well as their receiver type will be analyzed in order to infer any pattern.

3.1 GPS L1, L2C i L2W

In this study it is important to mention the case of L1 and L2 signals used for the GPS constellation since they will have an impact on the conclusions.

As previously mentioned, GPS satellites transmit signals on L1 and L2. The C/A code and the precision (P) code modulate the L1 signal. The L2 signal is modulated by the P-code only. To prevent spoofing of the military P-code signals, an encrypted code, called the W code, which is not available to civilian users, is modulated by the Department of Defense with the publicly known P code on both L1 and L2 to provide the anti-spoofing Y-code [8].

Without knowledge of the Y-code, it has to be applied a codeless or a semi-codeless technique for the reconstruction of the L2 carrier phase.

Thus, in this study it has been analyzed the signals obtained in L1 but also those that come from satellites that work with L2C /L2W.

L2C is the second civilian GPS signal, designed specifically to meet commercial needs. Its name refers to the radio frequency used by the signal (1227 MHz, or L2) and the fact that it is for civilian use. Because it is accesible by civilians, L2C is exactly known for the receivers and they don't have to use part of L1 signal to reconstruct it.

As mentioned before, there are also military signals at the L2 frequency, not published to civilian users. L2W has the encrypted Y-code that is unknown for the receivers. In light of this fact, manufacturers have made several options for L2W reconstruction, including the case of using together L1 and L2 for the reconstruction as it can be found in [8]. This will have an impact on the scintillation measurements that will be presented later.

From the table in the previous section, it can be inferred that all those available satellites can recover L2W, but eight can only work with L2W (they don't have L2C).

From now on, the reconstructed signal using together L1 and L2 is considered as the L2W signal.

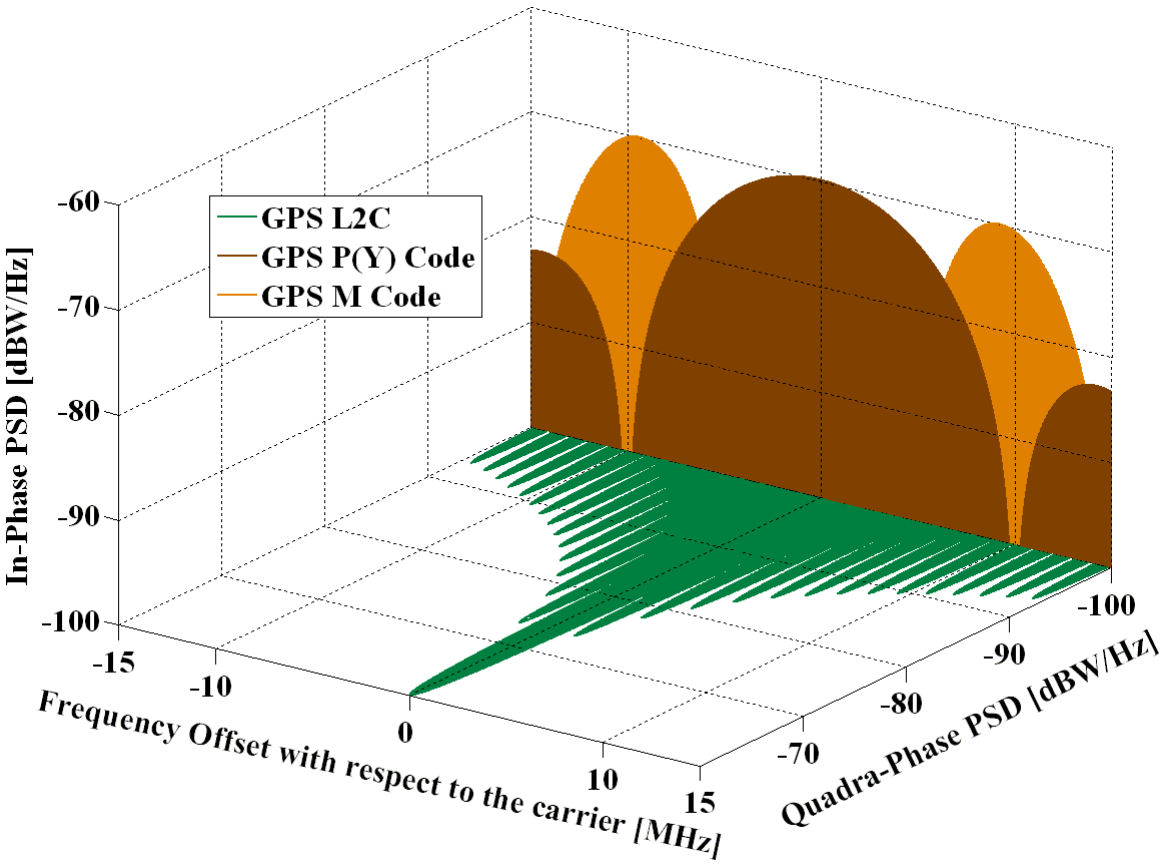

Figure 3.2: Spectra of the GPS Signals in L2 from [22]

Chapter 4

Selecting top scintillation days

This fifth chapter focuses on looking for those two days of the first 120 of 2020 with the greatest presence of scintillation and determining the stations that record it. It should be noted that this analysis will be done for both the GPS, Galileo and Glonass constellations.

4.1 Scintillation thresholds

4.1.1 ITM2020 thresholds

In order to determine which days have a greater presence of scintillation, limits must be established. These limits arise from the statistical study done in [21].

This study uses also the conventional geodetic receivers with a sampling frequency of 1 Hz that belong to the IGS network. The derivation of S_4 (amplitude scintillation) and σ_ϕ (phase scintillation) parameters uses a the exposed in Chapter 3 based in a precise GD of the carrier-phase measurements, as in PPP. Amplitude and phase scintillation have been described in Chapter 2 previously. In the study, they have been statistically characterized by means of the cumulative distribution functions (CDF) of S_4 and σ_ϕ results. Hence, for each satellite-receiver link, values are typically obtained every 1 min. S_4 and σ_ϕ values were calculated for all the days in two different years, 2007 and 2015 belonging, respectively, to low and high solar activity periods.

The study showed, for example, the 99% percentile in 2015 for low and high latitude receivers is typically in the range from 0.2 to 0.25 rad. Thus a threshold for moderate phase scintillation can be selected as a value equal to 0.25 rad. From the 99.9% percentile in 2015, one can fix a threshold for intense phase scintillation equal to 0.45 rad. Namely, values of σ_ϕ greater than 0.45 rad, which typically represent events with about 0.1% or smaller probability, are identified

as intense scintillation periods. In the same way, values of greater than 0.25 rad and smaller or equal than 0.45 rad, correspond to events with about 1% or smaller probability, and are identified as moderate scintillation periods.

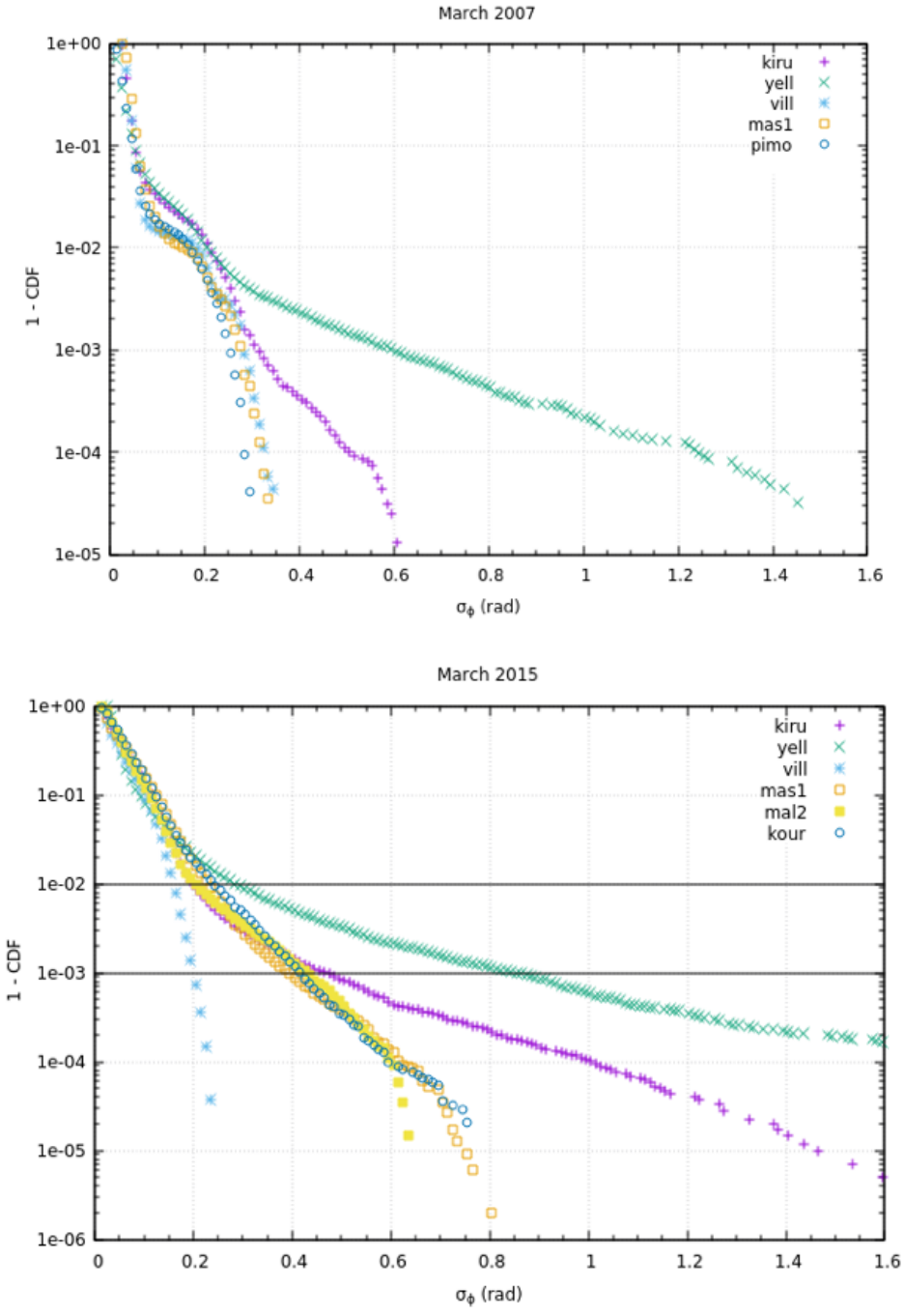

Figure 4.1: Complementary CDFs of σ_ϕ values for different receivers. Data from March 2007 (top) and March 2015 (bottom). Black horizontal lines indicate the 99% and 99.9% percentiles used to define moderate and intense phase scintillation thresholds from [21].

In the case of amplitude scintillation, a similar study as performed for σ_ϕ was repeated for the amplitude scintillation index S_4. Te thresholds for moderate and intense amplitude scintillation had been selected looking at the typical 99% and 99.9% percentiles of the different distributions during March 2015. From the CDFs of low latitude receivers one can take an S_4 value of 0.3 for the threshold of moderate amplitude scintillation, since it is representative of the 99% percentile of the low-latitude CDFs. On the other hand, a value of 0.5 is representative of the 99.9% percentile and is taken as the threshold for intense amplitude scintillation.

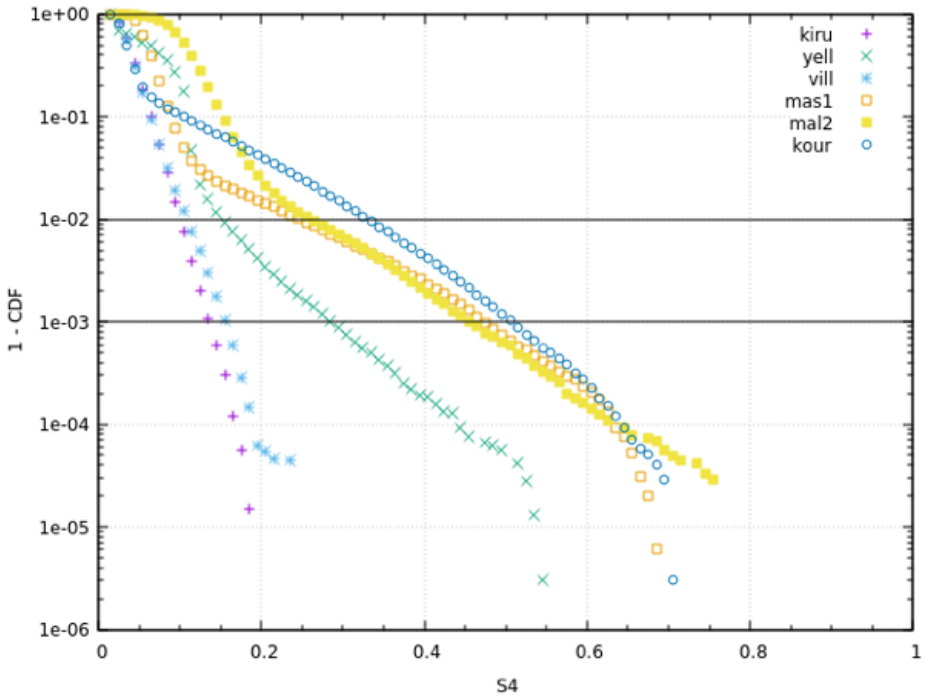

Figure 4.2: Complementary CDFs of S_4 values for different receivers from data in March 2015. Black horizontal lines indicate the 99% and 99.9% percentiles used to define moderate and intense amplitude scintillation thresholds. from [21].

The following table summarizes the trhesholds established for the phase and amplitude scintillation:

	σ_ϕ	S_4
Moderate	0.25 rad	0.3
Intensive	0.45 rad	0.5

Table 4.1: ITM2020 thresholds

4.1.2 ICAO trhesholds

The International Civil Aviation Organization (ICAO) is a United Nations agency established in 1944 by the Chicago Convention to study the problems of international civil aviation and to promote unique regulations and rules in the field of world aeronautics. Thus, this institution is quite important in the aerial field of satellite navigation.

In [17], another trhesholds for amplitude and phase scintillation are considered as a various types of space weather events affecting aviation:

		Moderate	*Severe*
GNSS			
	Amplitude Scintillation (S4)(dimensionless)	0.5	0.8
	Phase Scintillation (Sigma-Phi)(radians)	0.4	0.7
	Vertical TEC (TEC Units)	125	175
RADIATION			
	Effective Dose (micro-Sieverts/hour)*	30	80
HF			
	Auroral Absorption (Kp)	8	9
	PCA (dB from 30MHz Riometer data)	2	5
	Solar X-rays (0.1 - 0.8 nm)($W\text{-}m^{-2}$)	$1X10^{-4}$ (X1)	$1X10^{-3}$ (X10)
	Post-Storm Depression (MUF)**	30%	50%

Figure 4.3: Thresholds for space weather advisory from [17]

In this case, the thresholds for phase and amplitude scintillation are not specified where they are obtained from.

The study carried on in this project takes into account and compares the two different tresholds presented before.

However, in [21] only results from satellites belonging to the GPS constellation are considered, and an elevation mask of 30° had been applied for the derivation of scintillation parameters, in order to mitigate effects at low elevation in the results.

4.2 Top Days of Scintillation Results

In the case of this project, the results displayed are from satellites belonging to the GPS constellation but also to Galileo and Glonass.

The results obtained for each pair of station and day are shown below in the form of number of times in the day that each of the tresholds has been exceeded. The stations and days involved have been explained in Chapter 4. Stations are listed according to their Modified Dip Latitude (MODIP).

In order to analyze the first 120 days of 2020, two variables related to scintillation have been used, on the one hand, the parameter S_4 - which is the amplitude scintillation - and on the other hand, the $\sigma\phi_{L1}$, which is the phase scintillation.

4.2.1 Case GRE - All Constellations

This results contain the different satellites found in the GPS constellation, but also in Galileo and Glonass.

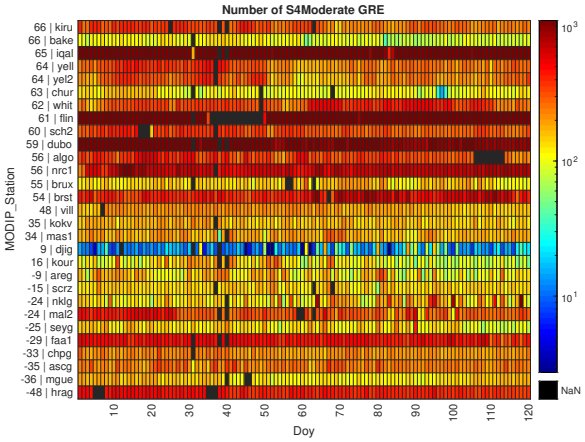

(a) Times S_4 Moderate - ITM2020 thresholds

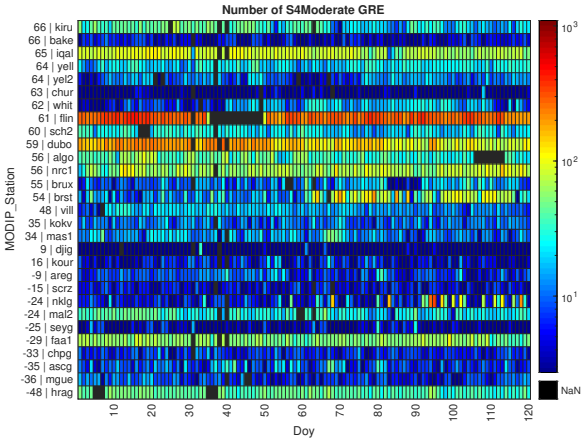

(b) Times S_4 Moderate - ICAO thresholds

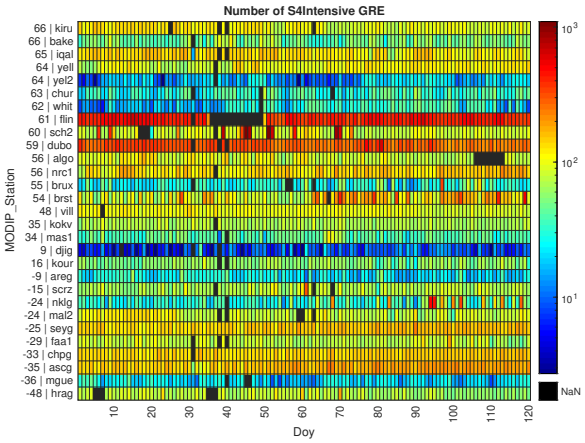

(c) Times S_4 Intensive - ITM2020 thresholds

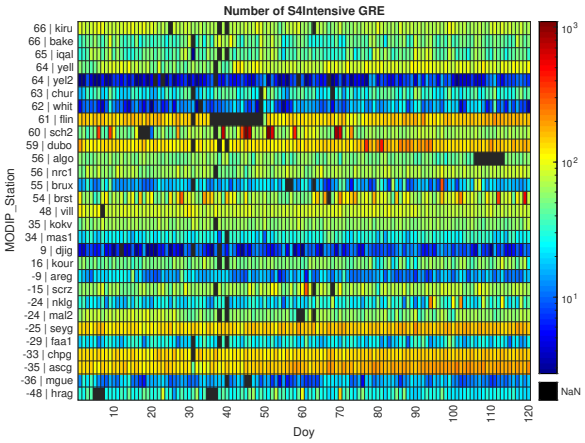

(d) Times S_4 Intensive - ICAO thresholds

Figure 4.4: Amplitude Scintillation S_4 incidence for GRE (All constellations)

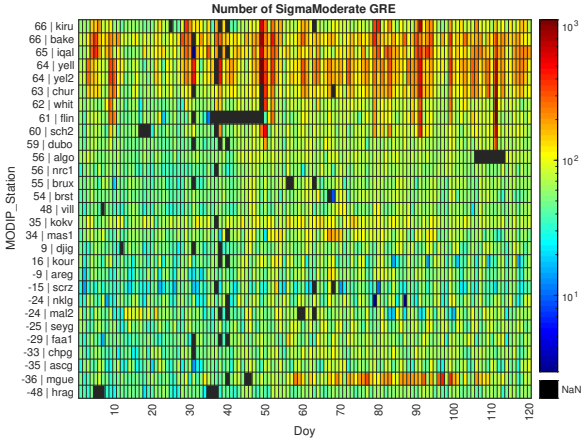

(a) Times $\sigma\phi$ Moderate - ITM2020 thresholds

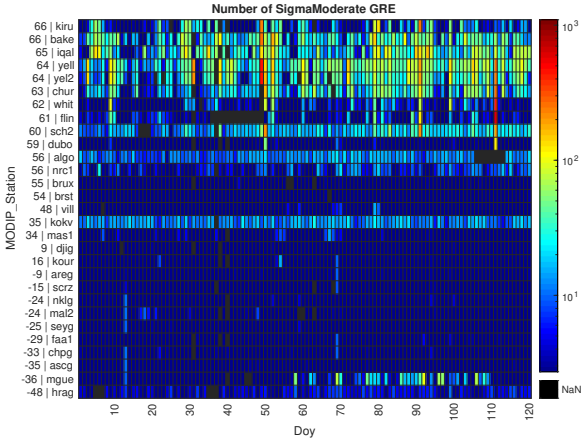

(b) Times $\sigma\phi$ Moderate - ICAO thresholds

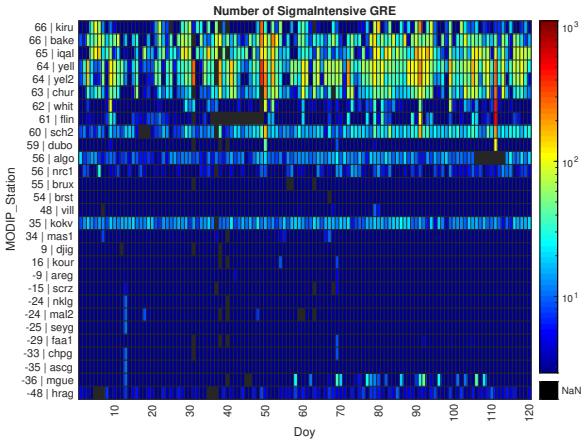

(c) Times $\sigma\phi$ Intensive - ITM2020 thresholds

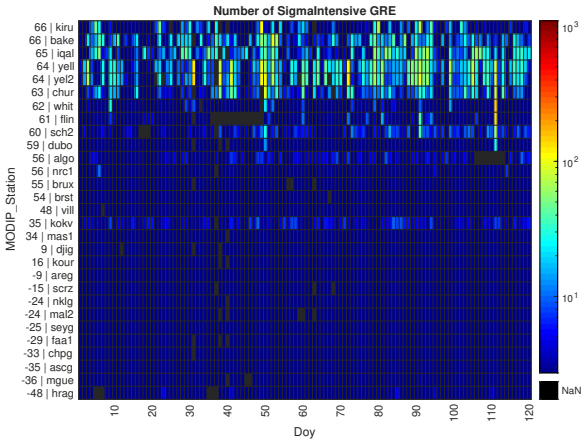

(d) Times $\sigma\phi$ Intensive - ICAO thresholds

Figure 4.5: Phase Scintillation $\sigma\phi$ incidence for GRE (All constellations)

In order to reduce noisy data from those satellites at low elevation, an elevation mask of 20° has been applied to mitigate the impact of worse modelling at low elevations in the following results.

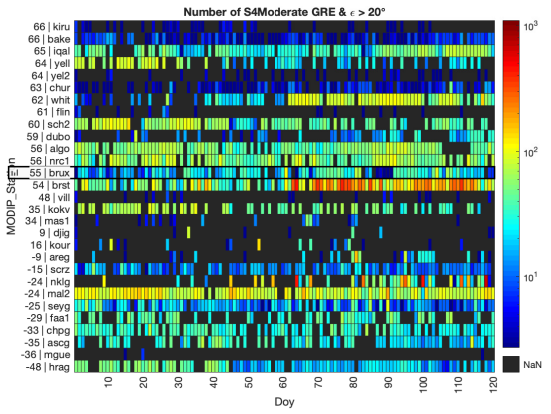

(a) Times S_4 Moderate - ITM2020 thresholds

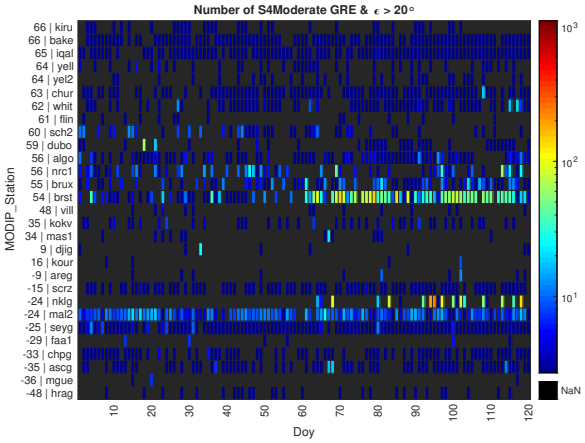

(b) Times S_4 Moderate - ICAO thresholds

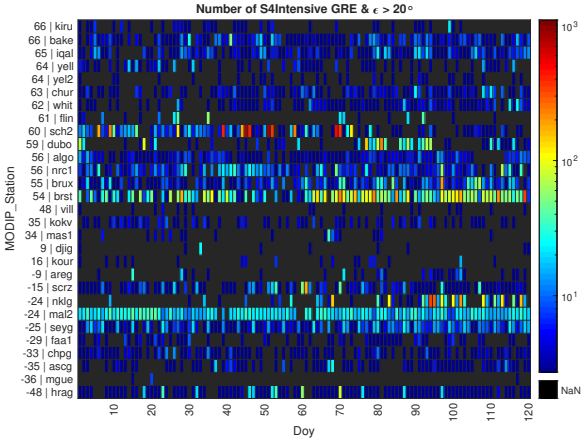

(c) Times S_4 Intensive - ITM2020 thresholds

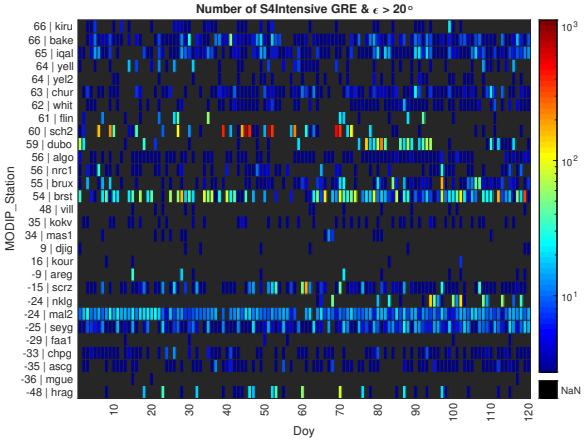

(d) Times S_4 Intensive - ICAO thresholds

Figure 4.6: Amplitude Scintillation S_4 incidence for GRE (All constellations) with $\epsilon > 20°$

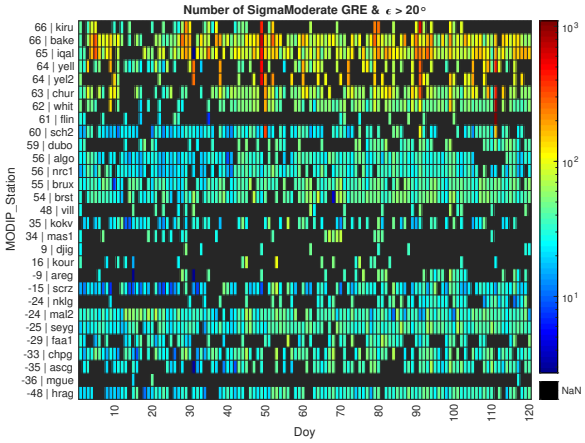

(a) Times $\sigma\phi$ Moderate - ITM2020 thresholds

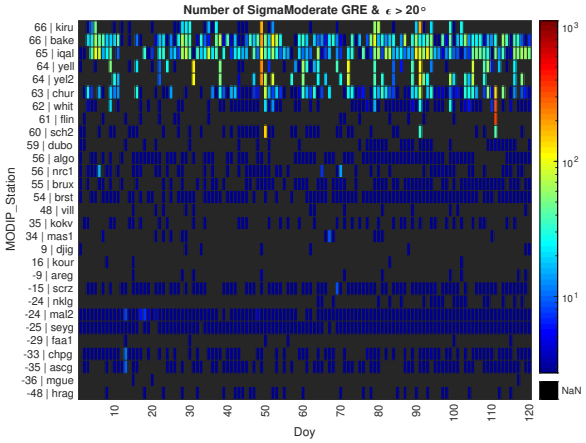

(b) Times $\sigma\phi$ Moderate - ICAO thresholds

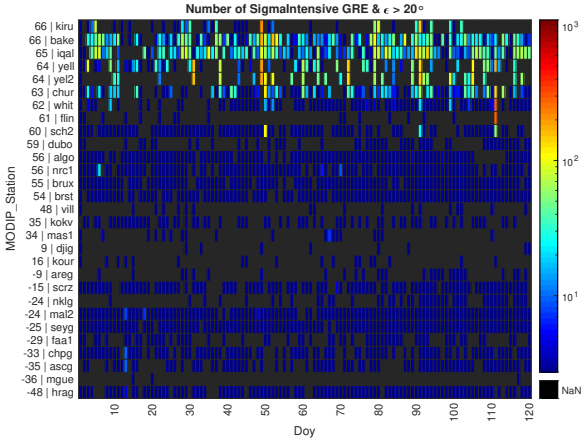

(c) Times $\sigma\phi$ Intensive - ITM2020 thresholds

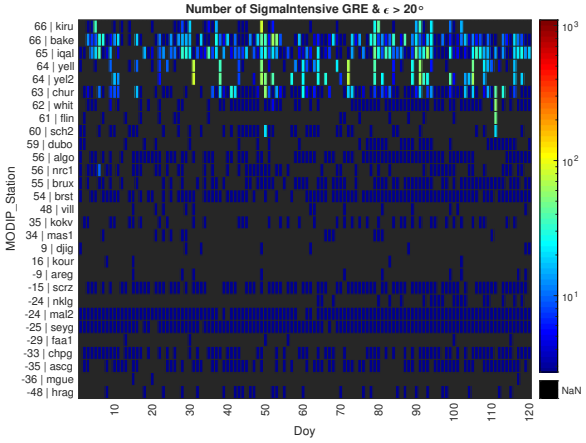

(d) Times $\sigma\phi$ Intensive - ICAO thresholds

Figure 4.7: Phase Scintillation $\sigma\phi$ incidence for GRE (All constellations) with $\epsilon > 20°$

4.2.2 Case GPS (G)

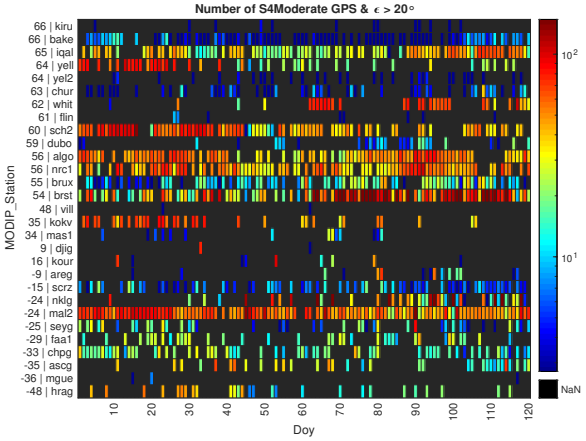

(a) Times S_4 Moderate - ITM2020 thresholds

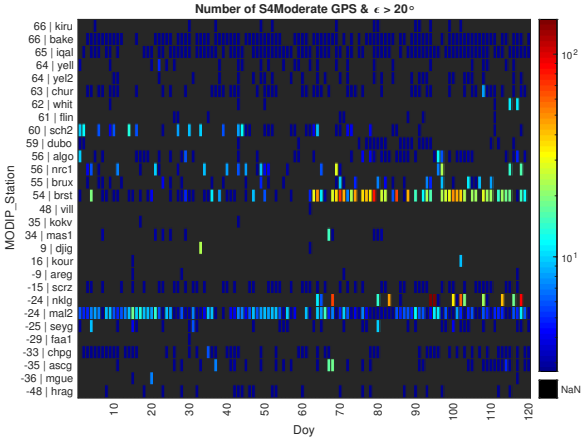

(b) Times S_4 Moderate - ICAO thresholds

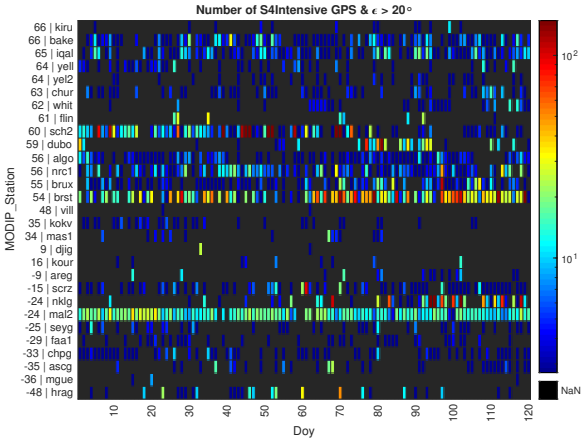

(c) Times S_4 Intensive - ITM2020 thresholds

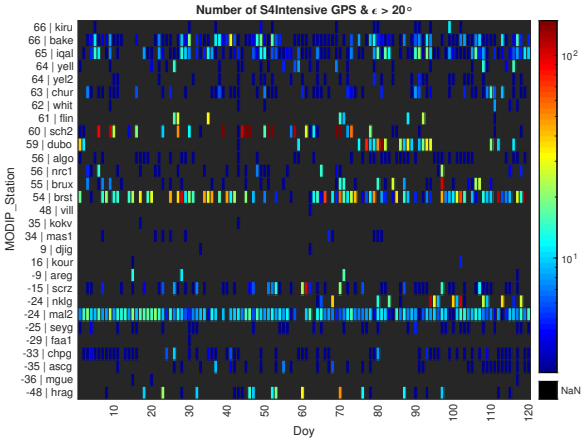

(d) Times S_4 Intensive - ICAO thresholds

Figure 4.8: Amplitude Scintillation S_4 incidence for GPS with $\epsilon > 20°$

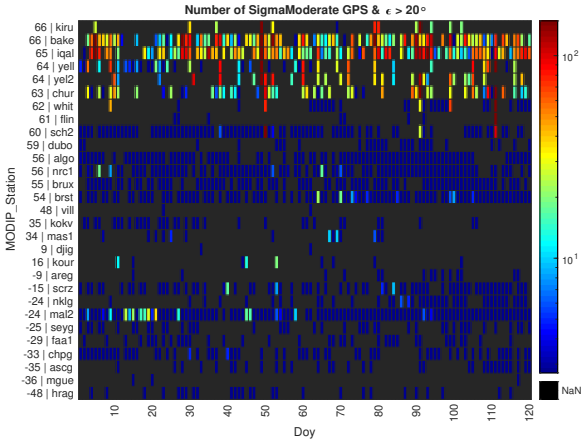

(a) Times $\sigma\phi$ Moderate - ITM2020 thresholds

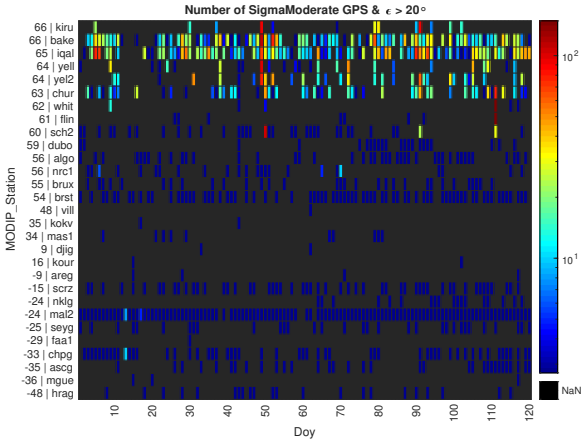

(b) Times $\sigma\phi$ Moderate - ICAO thresholds

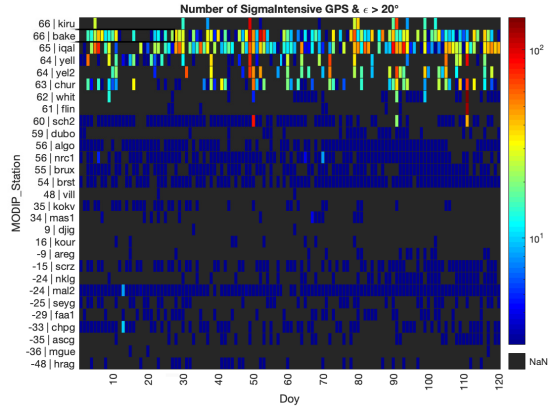

(c) Times $\sigma\phi$ Intensive - ITM2020 thresholds

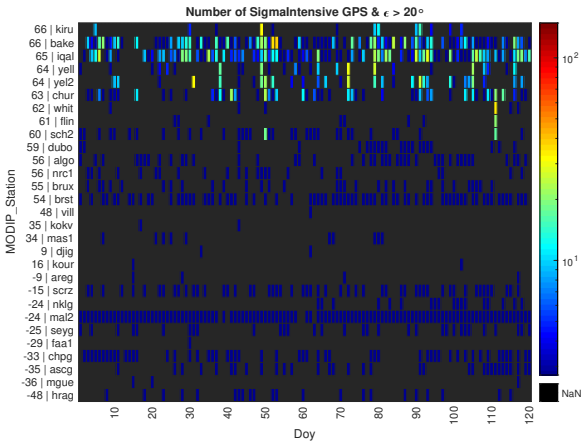

(d) Times $\sigma\phi$ Intensive - ICAO thresholds

Figure 4.9: Phase Scintillation $\sigma\phi$ incidence for GPS with $\epsilon > 20°$

4.2.3 Case GL0 (R)

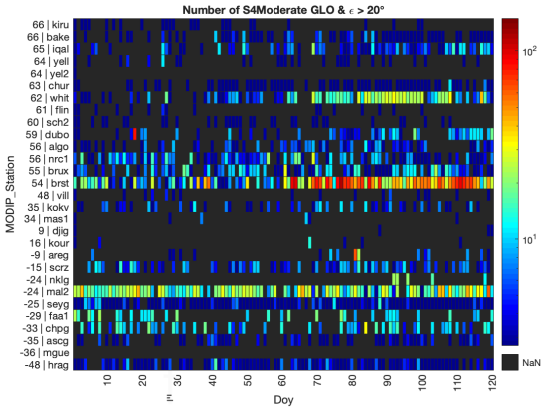

(a) Times S_4 Moderate - ITM2020 thresholds

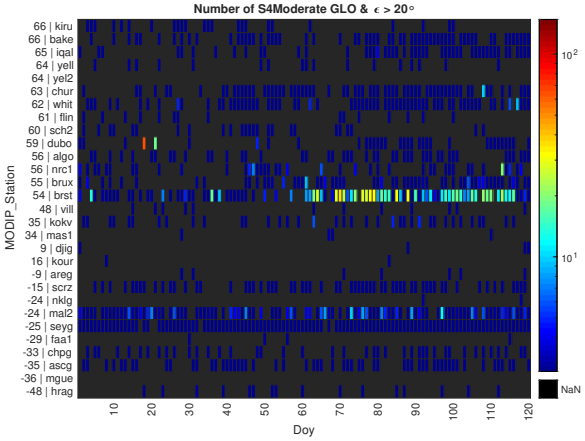

(b) Times S_4 Moderate - ICAO thresholds

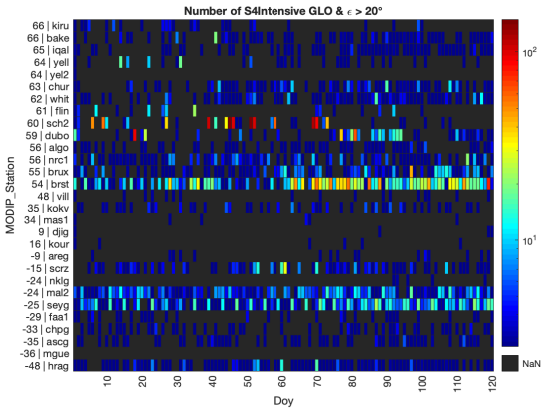

(c) Times S_4 Intensive - ITM2020 thresholds

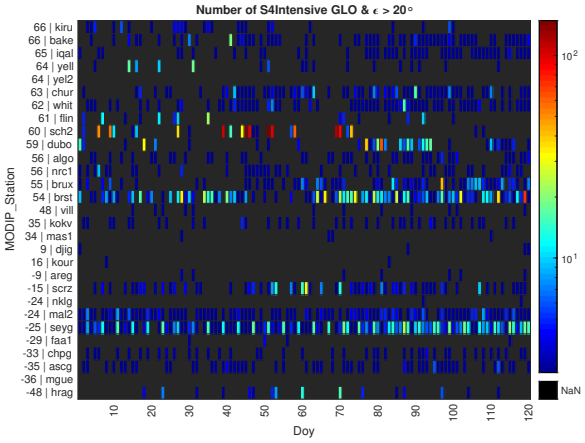

(d) Times S_4 Intensive - ICAO thresholds

Figure 4.10: Amplitude Scintillation S_4 incidence for GLO with $\epsilon > 20°$

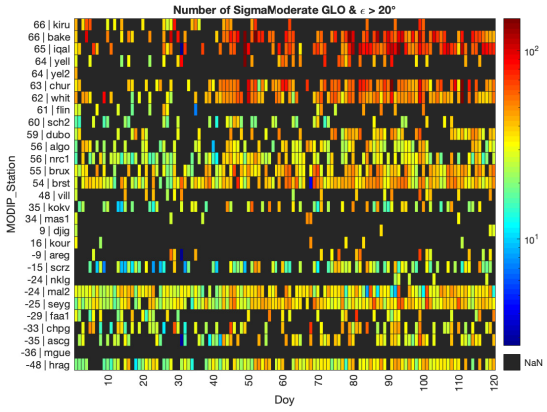

(a) Times $\sigma\phi$ Moderate - ITM2020 thresholds

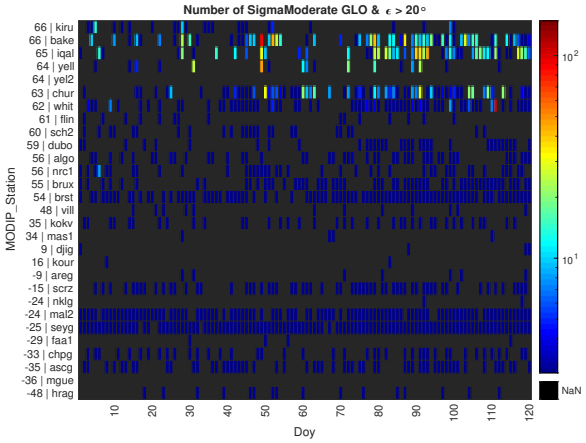

(b) Times $\sigma\phi$ Moderate - ICAO thresholds

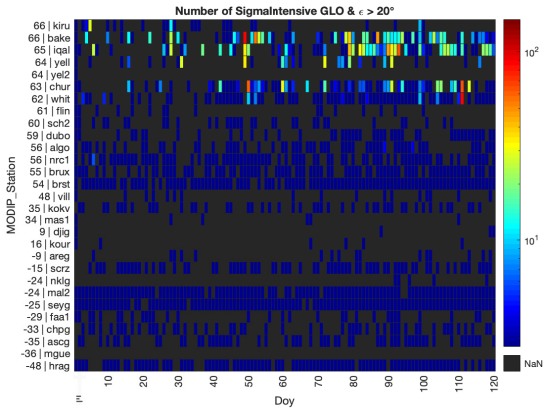

(c) Times $\sigma\phi$ Intensive - ITM2020 thresholds

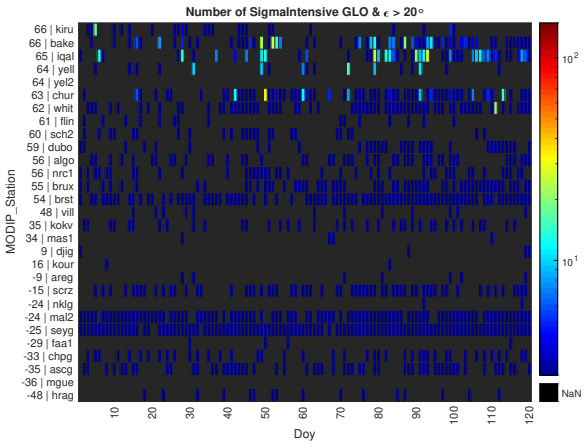

(d) Times $\sigma\phi$ Intensive - ICAO thresholds

Figure 4.11: Phase Scintillation $\sigma\phi$ incidence for GLO with $\epsilon > 20°$

4.2.4 Case GAL (E)

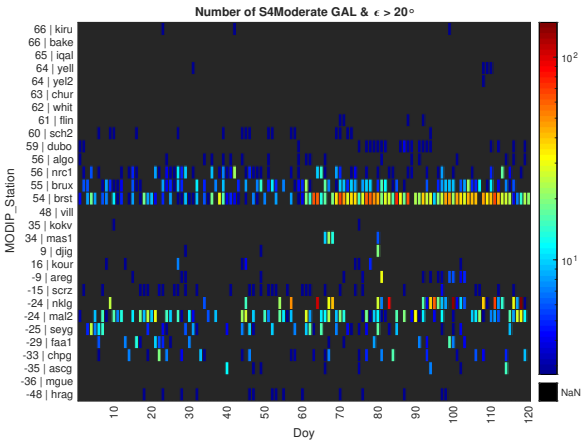

(a) Times S4 Moderate - ITM2020 thresholds

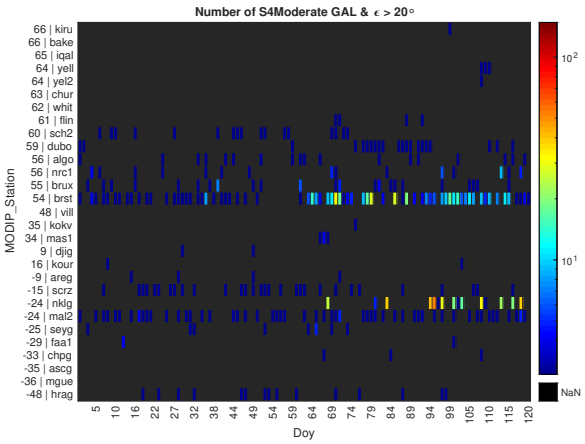

(b) Times S_4 Moderate - ICAO thresholds

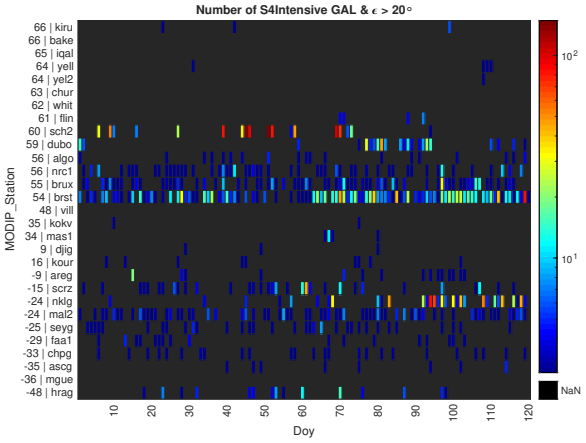

(c) Times S_4 Intensive - ITM2020 thresholds

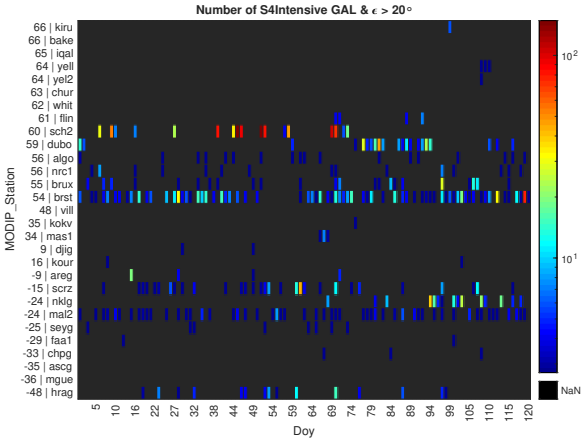

(d) Times S_4 Intensive - ICAO thresholds

Figure 4.12: Amplitude Scintillation S_4 incidence for GAL with $\epsilon > 20°$

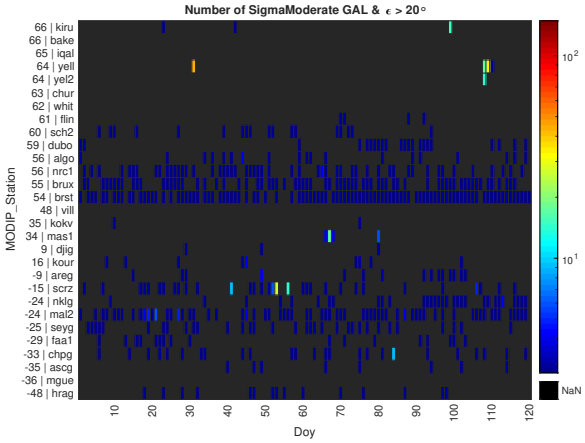

(a) Times $\sigma\phi$ Moderate - ITM2020 thresholds

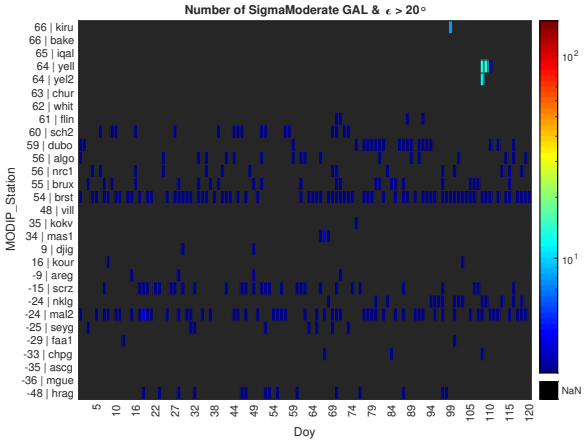

(b) Times $\sigma\phi$ Moderate - ICAO thresholds

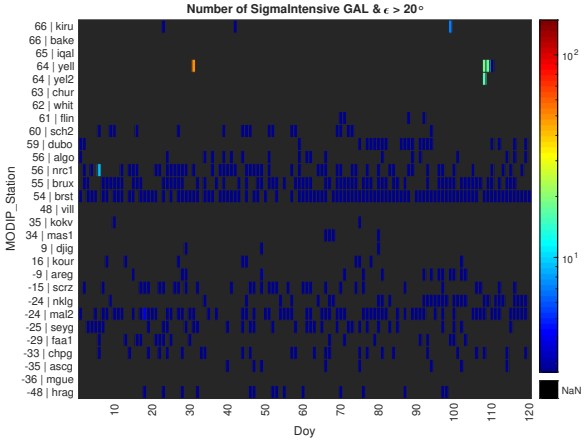

(c) Times $\sigma\phi$ Intensive - ITM2020 thresholds

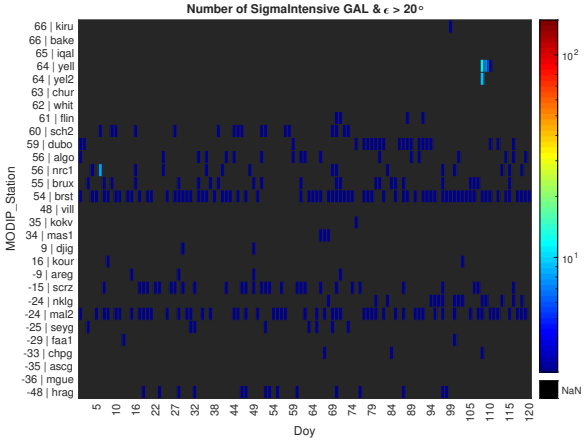

(d) Times $\sigma\phi$ Intensive - ICAO thresholds

Figure 4.13: Phase Scintillation $\sigma\phi$ incidence for GAL with $\epsilon > 20°$

4.2.5 Case GPS L2C

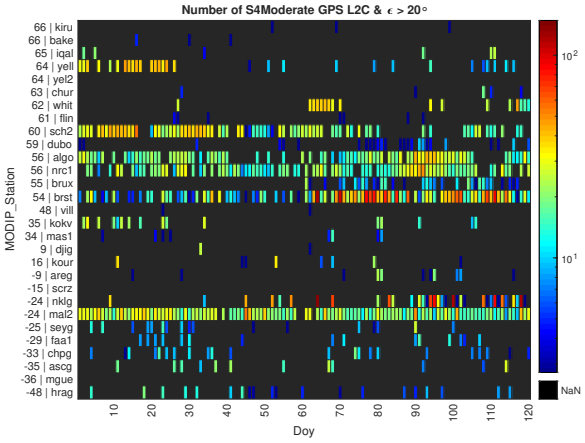

(a) Times S_4 Moderate - ITM2020 thresholds

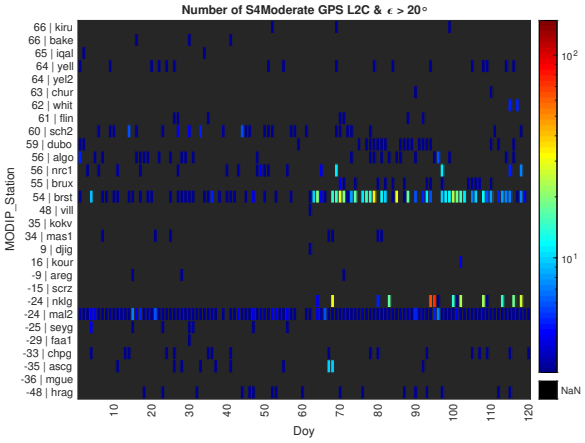

(b) Times S_4 Moderate - ICAO thresholds

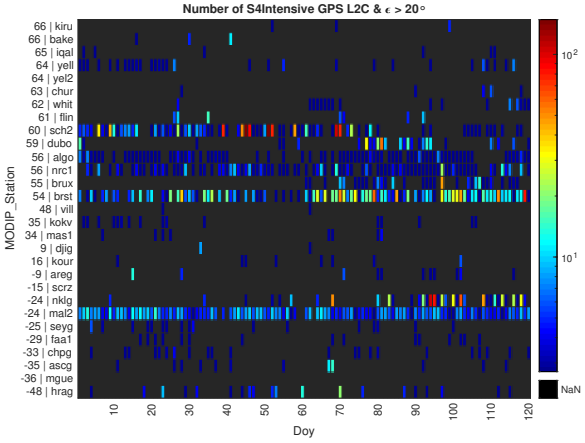

(c) Times S_4 Intensive - ITM2020 thresholds

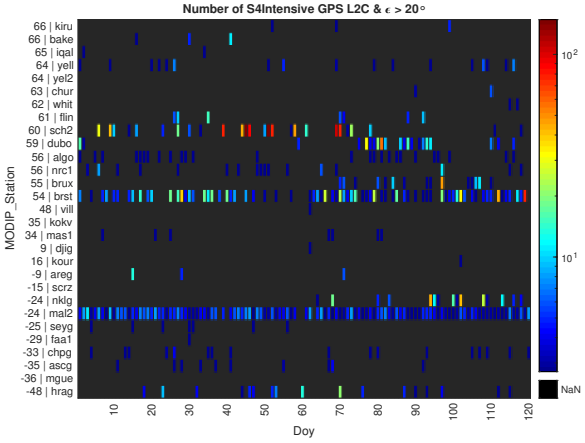

(d) Times S_4 Intensive - ICAO thresholds

Figure 4.14: Amplitude Scintillation S_4 incidence for GPS L2C with $\epsilon > 20°$

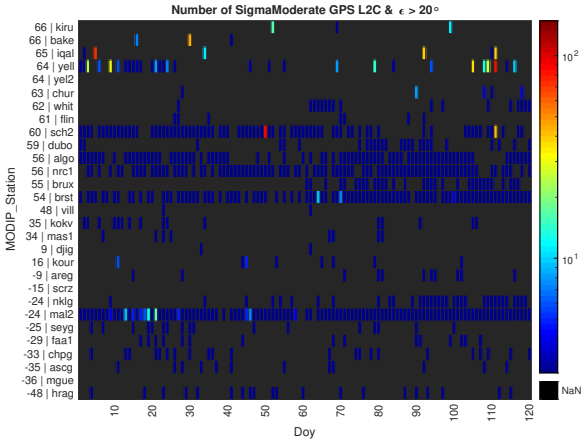

(a) Times $\sigma\phi$ Moderate - ITM2020 thresholds

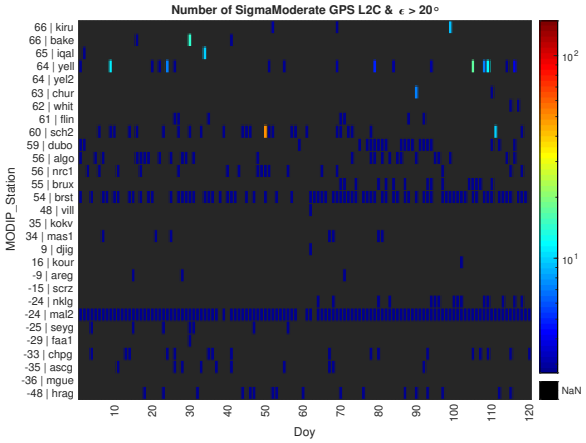

(b) Times $\sigma\phi$ Moderate - ICAO thresholds

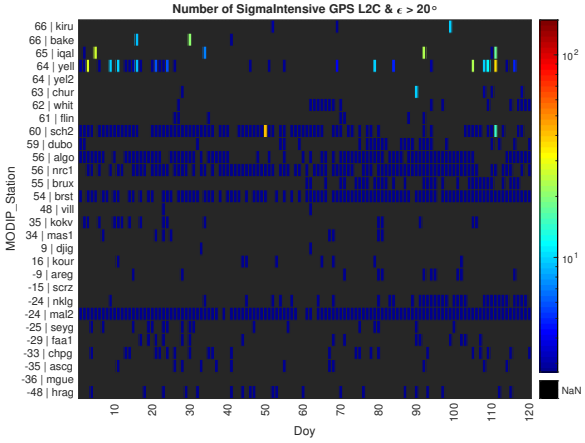

(c) Times $\sigma\phi$ Intensive - ITM2020 thresholds

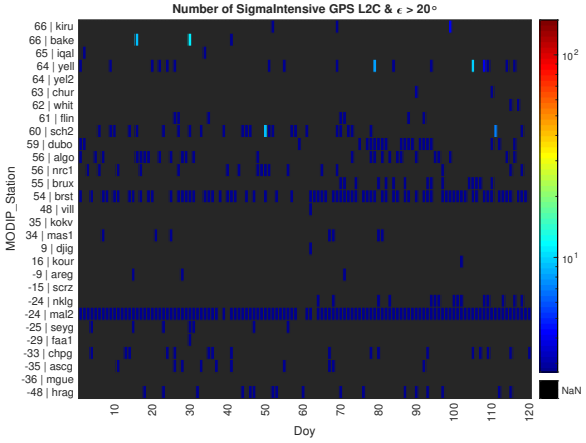

(d) Times $\sigma\phi$ Intensive - ICAO thresholds

Figure 4.15: Phase Scintillation $\sigma\phi$ incidence for GPS L2C with $\epsilon > 20°$

4.2.6 Case GPS L2W

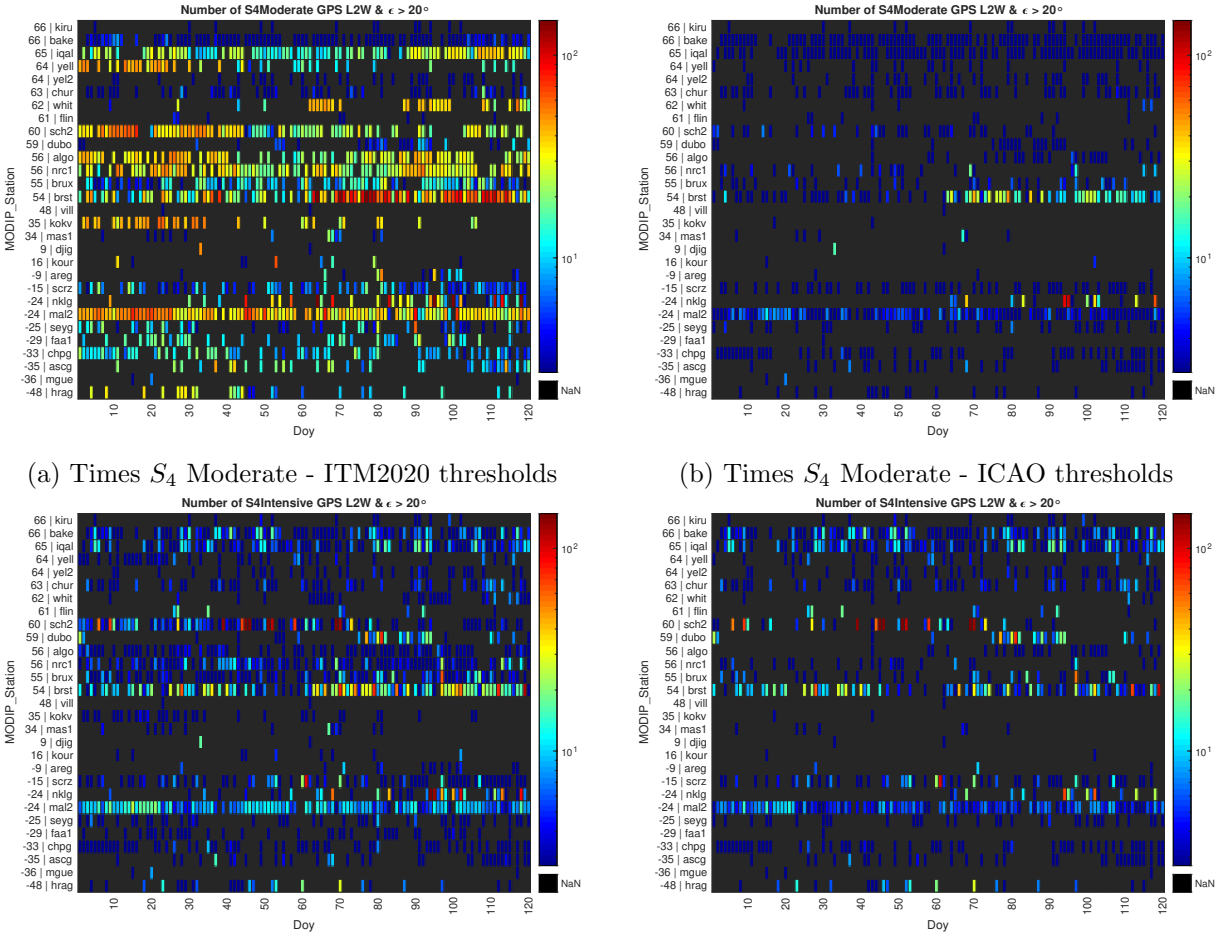

(a) Times S_4 Moderate - ITM2020 thresholds

(b) Times S_4 Moderate - ICAO thresholds

(c) Times S4 Intensive - ITM2020 thresholds

(d) Times S_4 Intensive - ICAO thresholds

Figure 4.16: Amplitude Scintillation S_4 incidence for GPS L2W with $\epsilon > 20°$

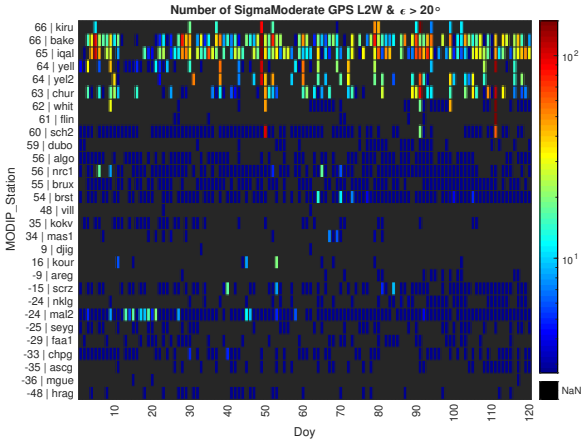

(a) Times $\sigma\phi$ Moderate - ITM2020 thresholds

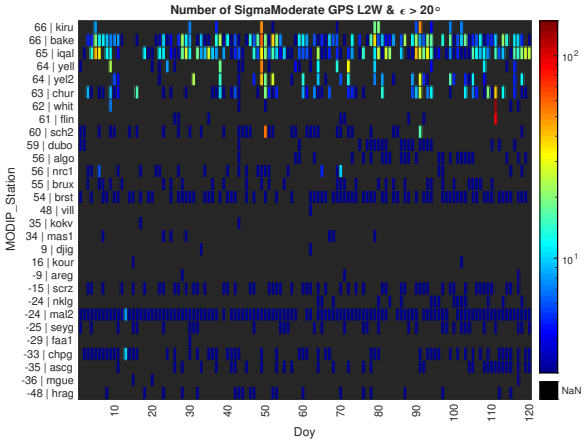

(b) Times $\sigma\phi$ Moderate - ICAO thresholds

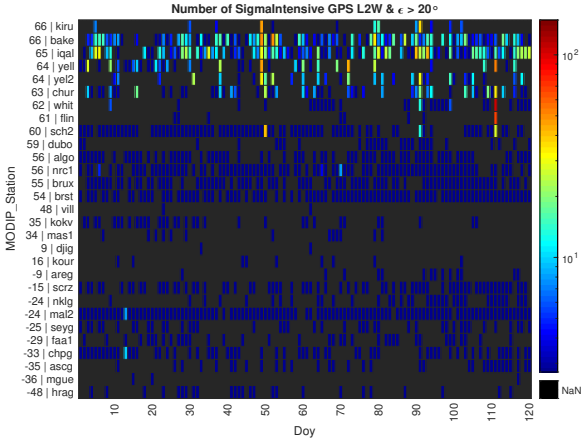

(c) Times $\sigma\phi$ Intensive - ITM2020 thresholds

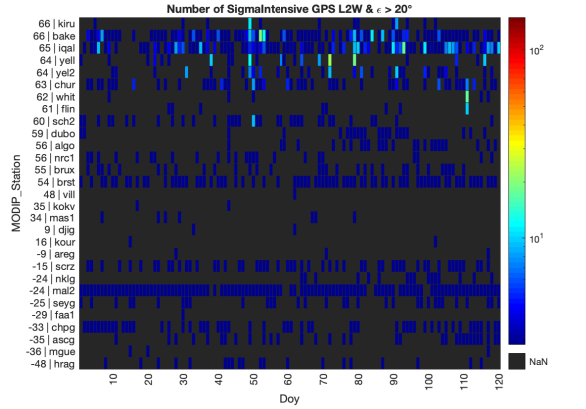

(d) Times $\sigma\phi$ Intensive - ICAO thresholds

Figure 4.17: Phase Scintillation $\sigma\phi$ incidence for GPS L2W with $\epsilon > 20°$

4.3 Analysis

It should be noted that the data provided by those satellites with an elevation less than 20 degrees have been removed. Only Fig 4.4 contains all the unfiltered data. Thus, this imposed mask cleanses the results by eliminating those that are more inaccurate due to the high noise content and worse modeling at low elevation, as it can be seen in Fig 4.5 compared to Fig. 4.4.

Twenty degrees has been chosen since it is a slightly higher altitude than the five degrees used for navigation and close to the 15 degrees that has been imposed in some studies carried out. It should be remembered that ISMR receivers apply masks up to 30 or 35 degrees.

Because 2020 is a year with little ionospheric activity, the previous graphs are represented on a logarithmic scale, to be able to differentiate with greater certainty those days with higher scintillation values. That is why the colors of the graphs of each constellation (excluding the unfiltered GRE case, Fig. 4.4, where all constellations are considered, are cold bluish tones).

From the results obtained taking into account all the constellations, that is, Fig 4.6 and 4.7, it can be seen that the variable S_4 does not provide relevant data (Fig 4.6) while the σ_ϕ considering the highest threshold, as "Sigma Intensive", it shows how clearly the scintillation is detected in the stations with a high latitude. This is reflected in images 4.7.c and 4.7.d.

It should be added that the results have been divided into their constellations in order to understand the contribution of each one to the GRE graph (Fig 4.8 and next).

The constellations separately also present the idea expressed above, the variable does not provide relevant data while the *"Sigma Moderate"* and even more, *"Sigma Intensive"*, determines that the scintillation occurs in the stations with higher latitude.

The GPS case is the one that most closely resembles the GRE case (Fig. 4.8 and 4.9). However, GLONASS charts are the ones with more warm colors. This does not mean that they are the ones that present more days with scintillation since the color of the graphs is due to the noise of the clocks and the satellite that appear as is it was scintillation. This is clearly shown in Fig 4.11.a. Therefore, the graphs of the GRE case are contaminated by the case. It can be concluded that GLONASS constellation data cannot be used as a robust scintillation indicator, due to inherent noise. This noise is due to the less stable clocks in GLO satellites.

On the opposite side, there are Galileo graphs that are very clean, there is less clock and receiver noise (Fig. 4.11 and 4.12). This is consistent with the more stable oscilators onboard the Galileo satellites that produce measurements with a reduced level of noise.

Finally, the study focuses on separating the GPS graphs in two. Those GPS that work with the L2C signal (Fig. 4.14 and Fig. 4.15) and those that work with the L2W signal (Fig. 5.16 and Fig. 4.17). As it can be seen, L2W graphs present higher noise since it depends on how the

receiver calculates the GPS signal differently. That is why stations located next to each other, at the same latitude, present different levels of scintillation.

As a first conclusion of this first study, it can be determined that the most reliable indicator of scintillation is the σ_ϕ and it is therefore on which the next studies will focus. On the other hand, if the GPS data is taken into account, due to both, the interest in the duality of having L2C and L2W, and more scintillation values detected, the two days with the most scintillation are day 49 and 111. So the next study will focus on those days and that constellation.

Chapter 5

Scintillation case study

This Chapter intends to take one more step in the study, to advance in its depth. That is why from the previous study, the two days are selected from among the 120 that suffer the most scintillation. These are days 49 and 111.

These days will be analyzed in detail in two stations taken consciously: yell and yel2.

The reasons for choosing these two stations are the following, which generate special interest for this study:

1. These two stations are located at high latitude where it has been shown in the previous Chapter that there are higher scintillation data.
2. These two stations are located at same latitude, therefore, the available satellites and the data collected should in principle be similar.
3. They are located very close, only a distance of 50 meters separates them.
4. However, the type of receiver for each station is different. The station shout uses a JAVAD type of receiver while yel2 uses SEPTENTRIO.

This last point, will give a new variable that comes into play, the type of receiver. It will be analyzed whether it affects the signals and therefore the scintillation data despite the fact that the scenario by the two stations is almost identical.

5.1 Data set Evaluated

In this case, as it is mentioned before, an analysis will be carried out on the 49th and the 111th of 2020, that is, 18th of February and 20th of April, for the pair of stations yel, yell2.

The data collected are those that arise from applying the geo-detreding approach explained in detail in the Chapter 2. The data collected has an interval of 1 minute or 60 seconds, from the first minute of the day (60) to the second 86040, which corresponds to 23.98 hours.

Likewise, the study focuses on the GPS constellation because it is the constellation that, according to the results of the previous Chapter, has more coherent and also notable scintillation values. Furthermore, this constellation has the peculiarity of containing the L1, L2C and L2W signals explained in Chapter 3. In addition, the study is carried out along the σ_ϕ values of L1 because in the previous Chapter this index has presented the scintillation data more consistently.

Regarding this last aspect, the daily results will be divided into two large blocks, the one formed by all the satellites that have L2W and the one formed by those satellites that apart from having L2W also have L2C.These second satellites correspond to higher blocks, that is, modern satellites. Again, a new variable, in this case the type of signal, comes into play and will be analyzed.

To mitigate the noise in the cintillation indices, as was done in the previous Chapter, only GPS satellites with an elevation greater than 20 degrees are listed.

5.2 Day 49 Results

Figure 5.1 depicts the results of day 49 for the two pairs of stations and the two blocks mentioned above. In a same column the station and therefore, the receiver is the same but it can be seen the comparation between the two blocks. In contrast, in a same row, same blocks are depicted but in different receivers/stations:

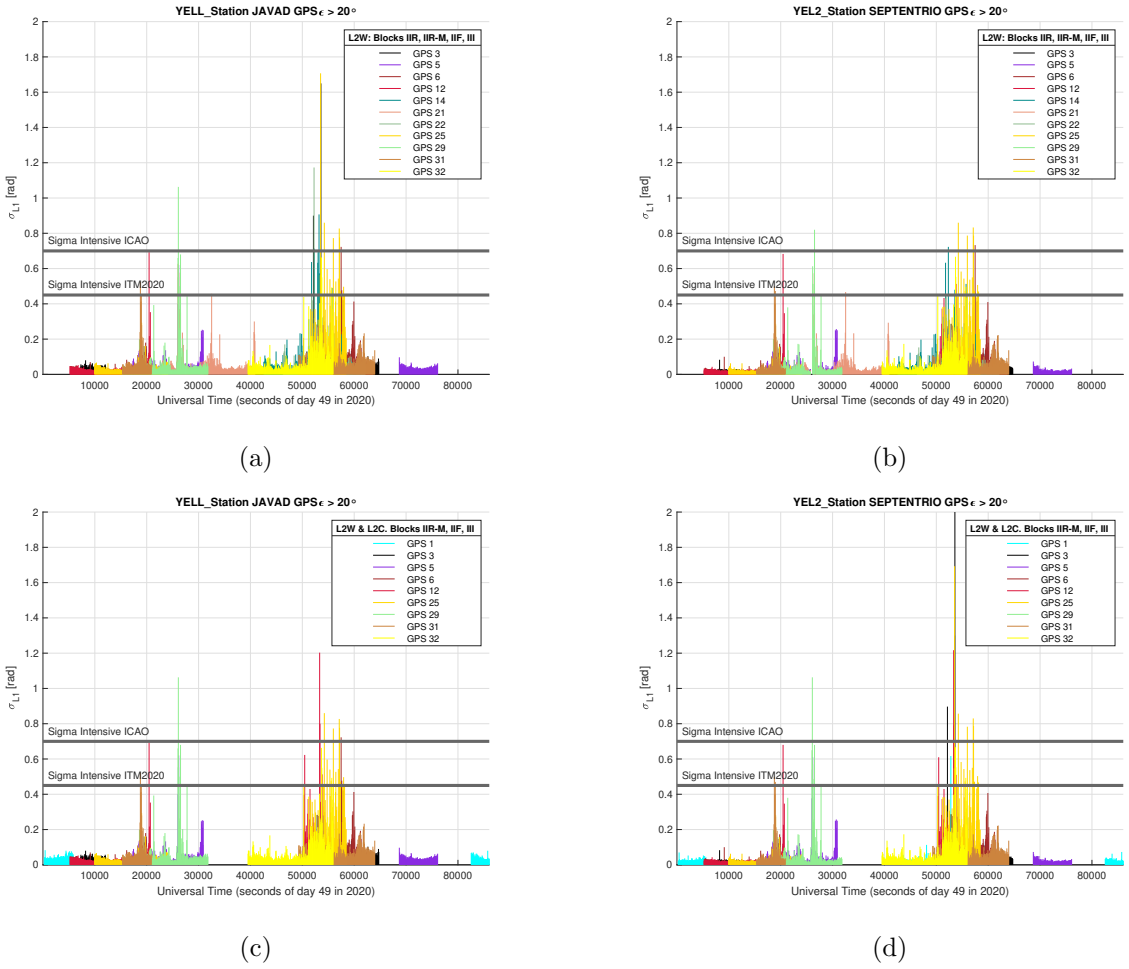

Figure 5.1: GPS Satellites on 49th Day od 2020

5.3 Day 111 Results

Below are the results of day 111 for the two pairs of stations and the two blocks mentioned above:

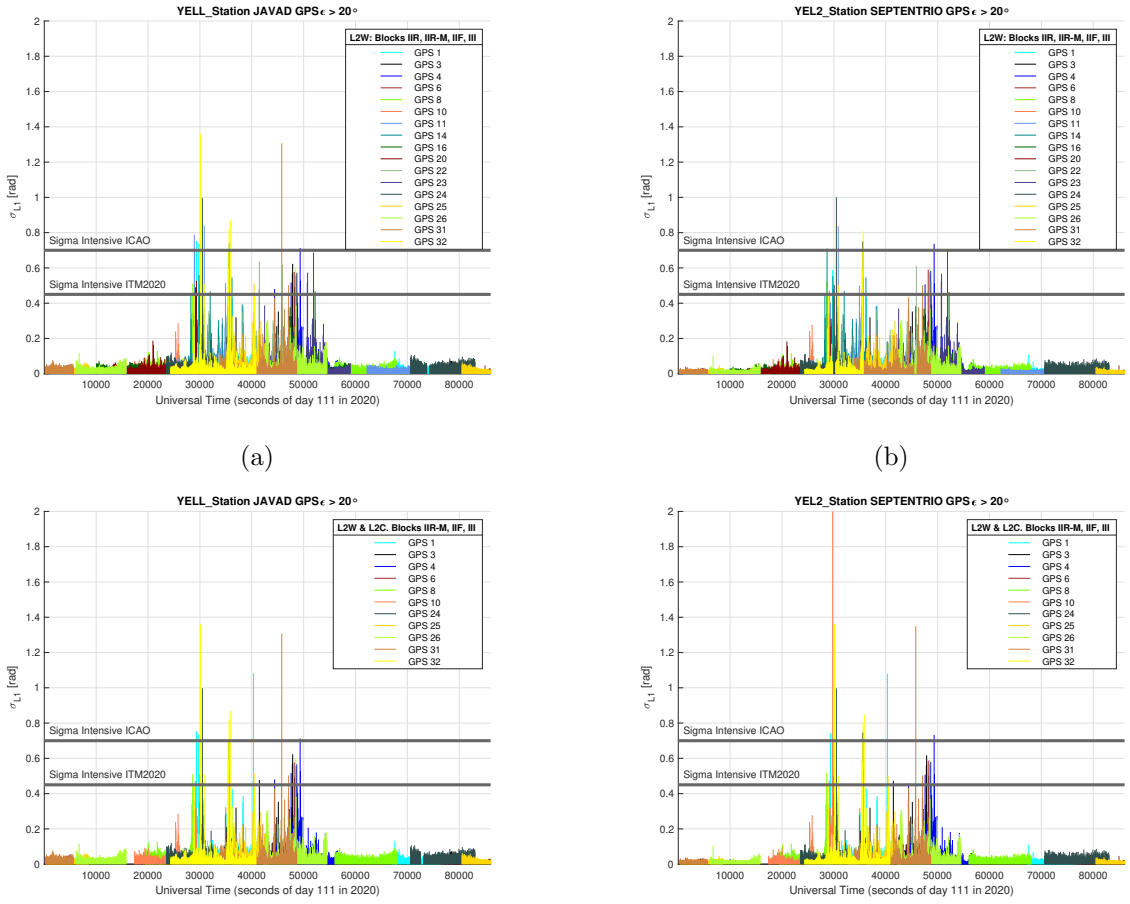

(a) (b)

(c) (d)

Figure 5.2: GPS Satellites on 111th Day of 2020

In the graphs shown, those satellites that have exceeded the ITM threshold in one of the two stations are represented. Likewise, the two horizontal lines shown correspond to both the ICAO and ITM thresholds explained in the Chapter 4.

As can be seen in all the graphs, the base noise of the SEPTENTRIO receiver when there is no scintillation is lower than the base noise presented by JAVAD receivers.

This fact can be seen in the first minutes of any graph of the two days represented.

If now the study focuses on day 49, the first two graphs show the behavior of the receivers that work with the L2W signal. As it can be seen, satellite 3 and 25 have very high scintillation data in JAVAD receivers but not in SEPTENTRIO receiver. This indicates that working with L2W, JAVAD receivers are more robust to scintillation and keep more signal tracking compared to SEPTENTRIO, which are not capable of tracking and they produce cycle-slips.

The same phenomenon also occurs on day 111 with GPS 32 (yellow) and 31 (brown) that appear in Fig. 5.2a but not in Fig. 5.2b.

However, if the signal block with L2C is observed (the graphs at the bottom of each page) SEPTENTRIO receiver is capable of handling the tracking of signals that disappear in the case of the JAVAD receiver.

This is what happens with GPS 3 on day 49, which has a high scintillation in Fig 5.1d and does not appear in Fig 5.1c. The same happens on day 111 with GPS 10 (in red) which has a high scintillation value in Fig. 5.2d but disappears in Fig. 5.2c.

Finally, if the signal tracking that the SEPTENTRIO receiver follows with the L2C block is compared to the signal tracking that the JAVAD receiver follows with the L2W ((a) and (d) graph of each day), it can be observed on both days that the SEPTENTRIO is able to record higher scintillation values of GPS signals that are lower or non-existent in the JAVAD receiver.

Chapter 6

Analysis of certain GPS on Day 49 and 111

This chapter tries to analyze with more caution those satellites that have presented a higher scintillation values on time intervals of days 49 and 111 in a shorter time interval than the previous one, that is, in hours.

This allows to reveal in a more way the behavior of these satellites from the point of view of the different receivers and signals involved.

GPS 3 and 25 of day 49 of 2020 and GPS 10 and 31 of day 111 are those that present the highest scintillation values of $\sigma_{\phi L1}$ during a certain time interval, and therefore, they will be the array of GPS satellites to be analyzed.

First, its behavior with respect to the scintillation variable $\sigma_{\phi L1}$ is analyzed.The analysis will continue with the combinations of signals where L2 intervenes, that is, σ_ϕ of Geometry Free,

$$L_{GF} = L1 - L2 \tag{6.1}$$

combination used in ionospheric analysis, and σ_ϕ of the Iono Free combination,

$$L_{IF} = \frac{f1^2 \cdot L1 - f2^2 \cdot L2}{f1^2 - f2^2} \tag{6.2}$$

combination used in precise navigation (PPP).

Because the physical signals are those that have lambda, but not the mathematical constructions, it is more correct to show the results of the different σ values in centimeters and not in radians as has been done up to now. That is why the following graphs show values in centimeters, making the conversion of $1rad = 0.03cm$.

RINEX format version 3 has added the capabilities of both the legacy L2P(Y), L2W in this case, and the modern L2C GPS carrrier phase. This makes it possible to work with both signals.

However, these two signals are not entirely interchangeable. In [14], a first clear difference between total electroc content (TEC) and ROTI index derived using the L2W observable and the L2C observable is observed. In addition, tracking the L2W signal requires using encryption. The widely used codeless or semi-codeless techniques rely heavily on the L1 signal in acquiring and tracking the L2W signal. This leads to high-frequency variations in the L2 carrier phase, which are heavily influenced by the L1 phase variations. In [16], it is confirmed that, in the case of Septentrio receivers, L2W carrier phase observable is influenced by the L1C/A-based carrier phase to the point that the high-frequency variations in L2W carrier phase measurements are nearly identical to those form the L1C/A signal.

6.1 $\sigma_{\phi L1}$ Analysis

6.1.1 Results

The results are shown below for each station-receiver pair for those time intervals where GPS 3 and GPS 25 have shown higher scintillation values according to the variable $\sigma_{\phi L1}$ on day 49.

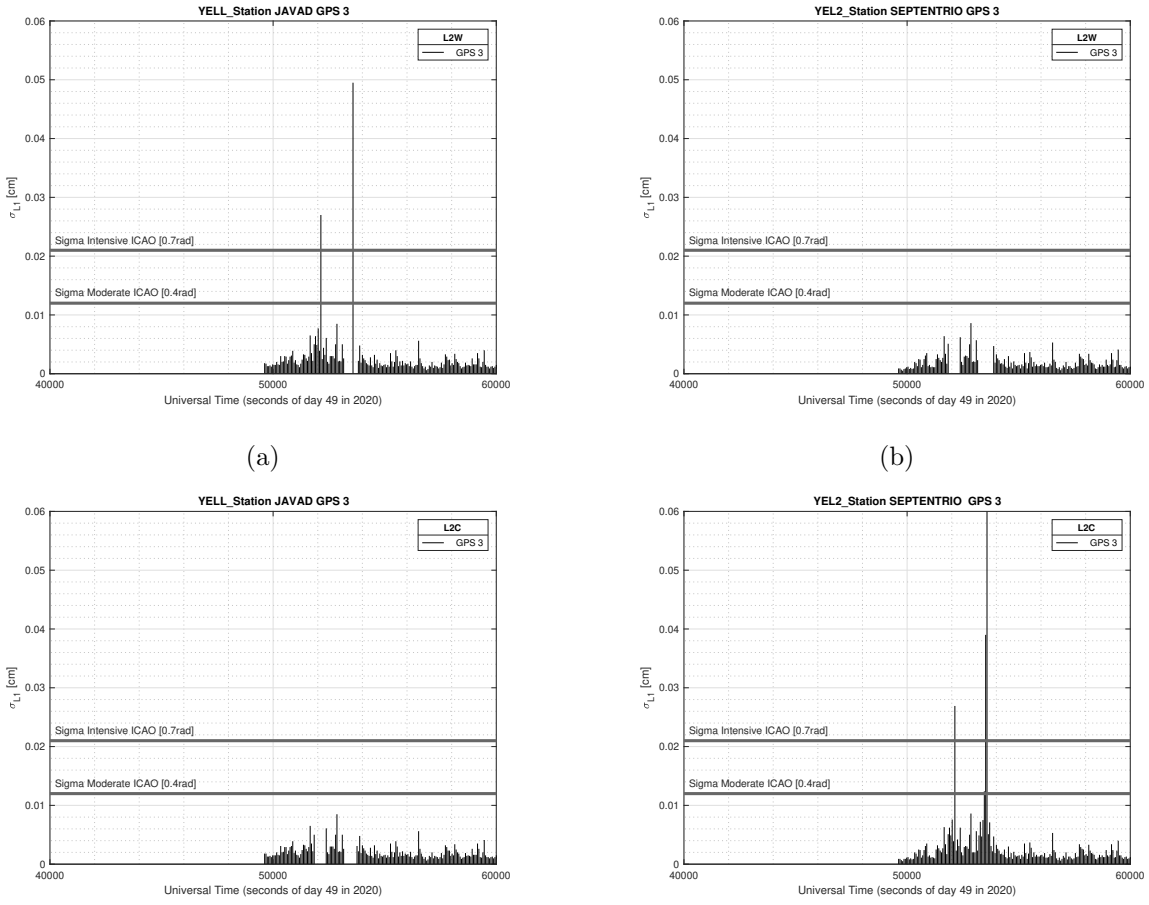

Figure 6.1: GPS 3 on 49th Day of 2020

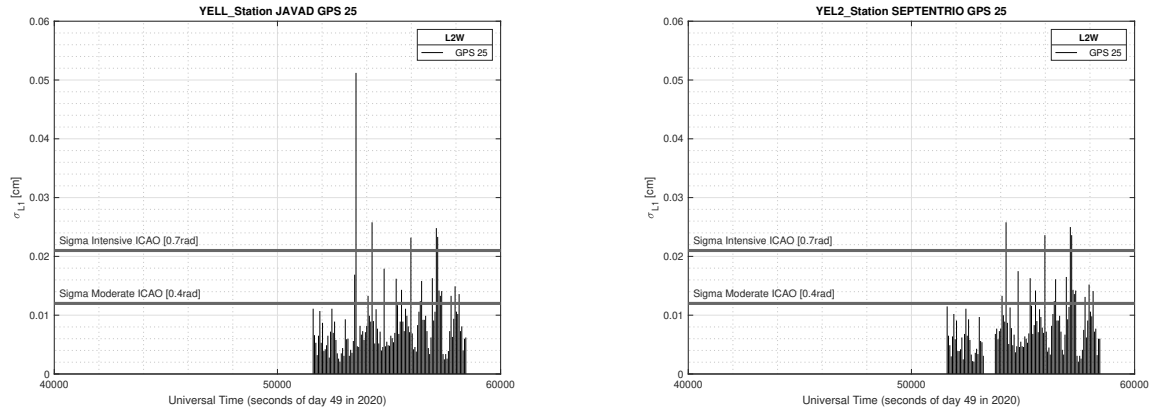

(a)

(b)

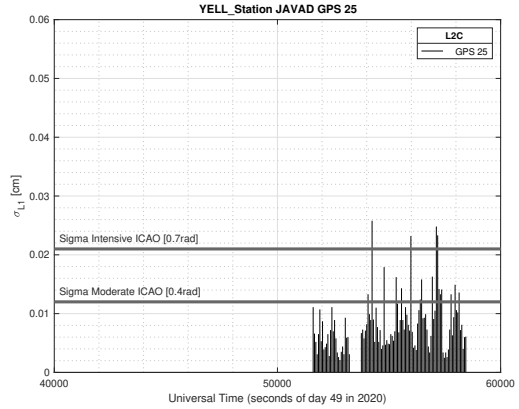

(c)

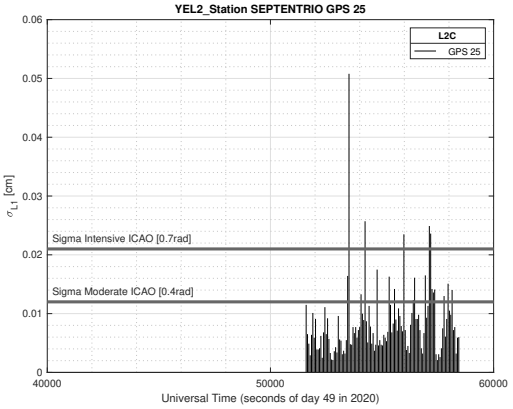

(d)

Figure 6.2: GPS 25 on 49th Day of 2020

After having analyzed in detail the two satellites that presented the highest scintillation on day 49, the study is carried out again, but in this case for the two satellites that present higher scintillation values on day 111.

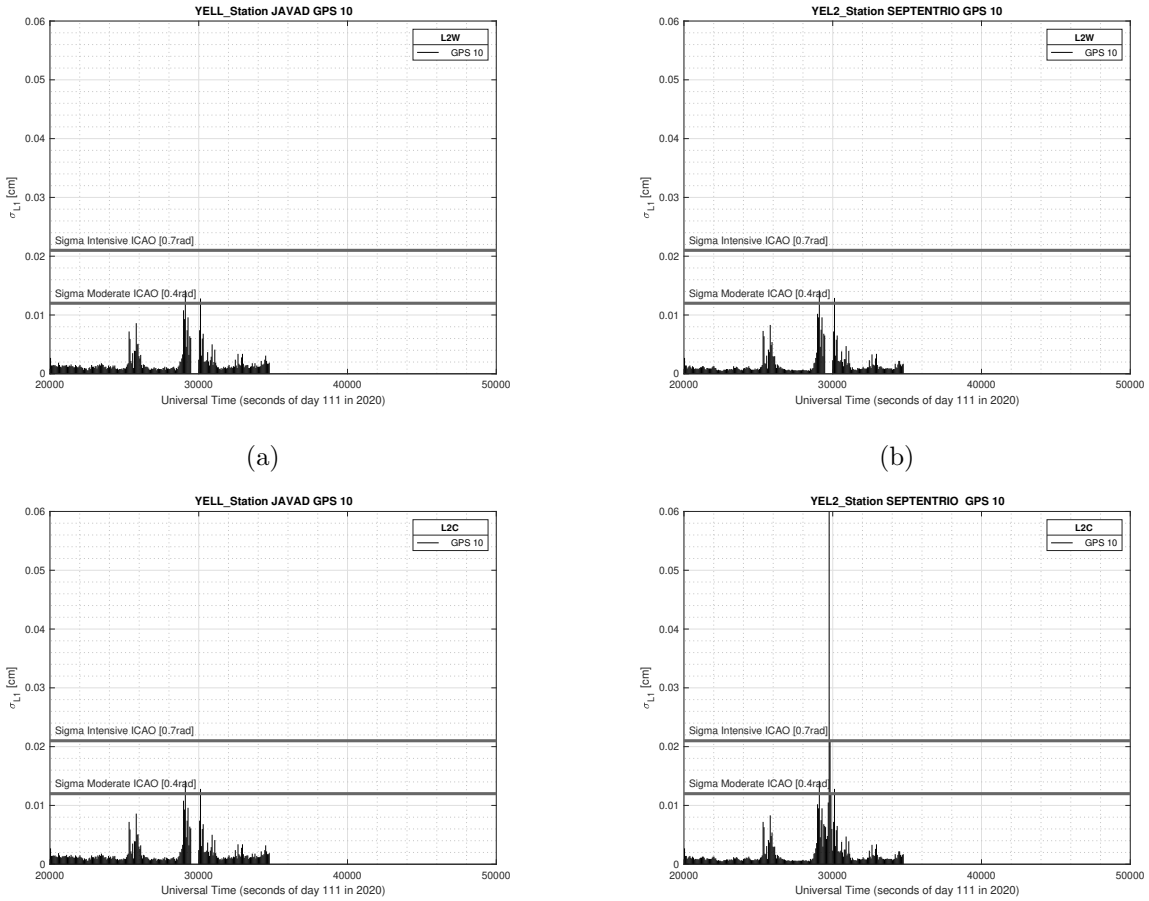

Figure 6.3: GPS 10 on 111th Day of 2020

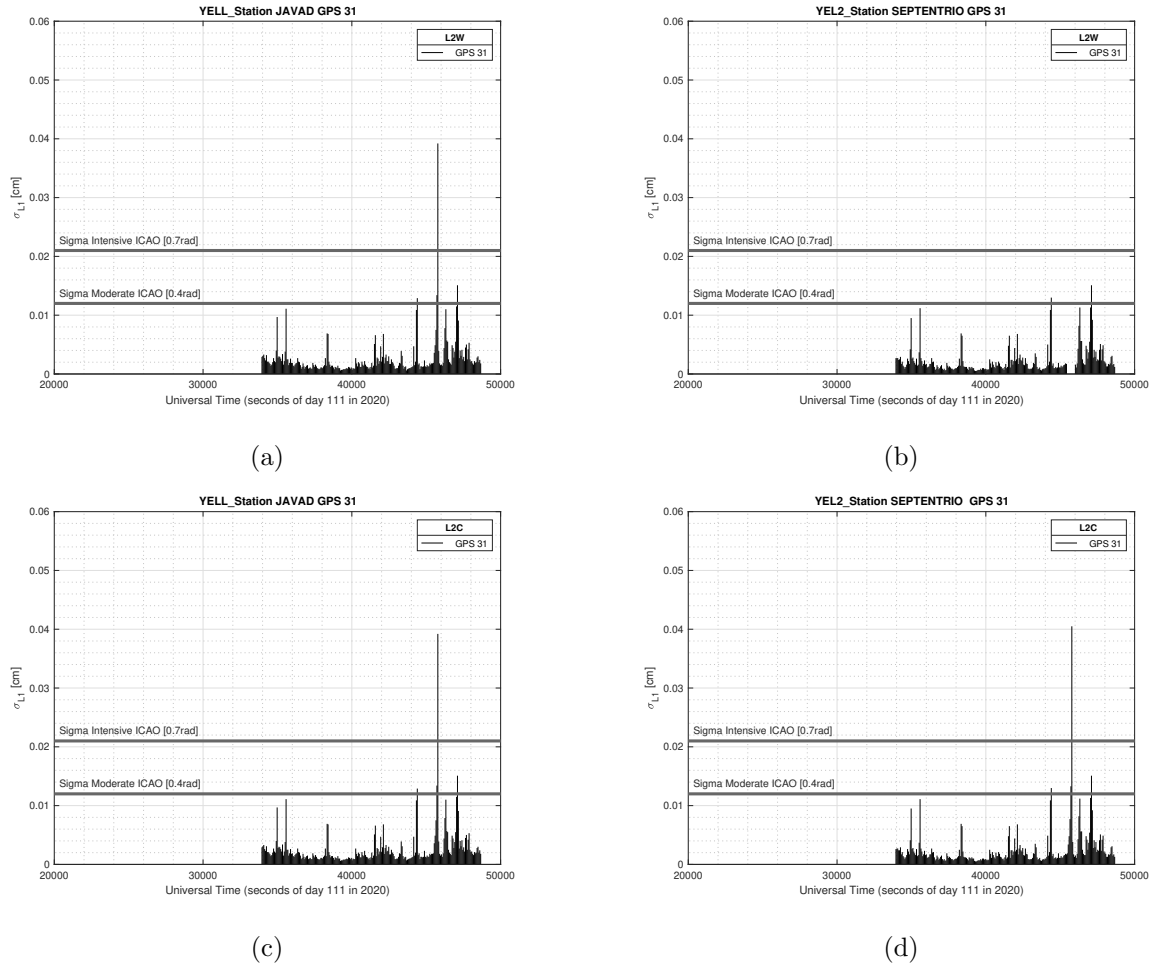

Figure 6.4: GPS 31 on 111th Day of 2020

Finally, the following images are attached, which are an overlay for each satellite of the four previous images. In this type of chart, data gaps look like straight lines.

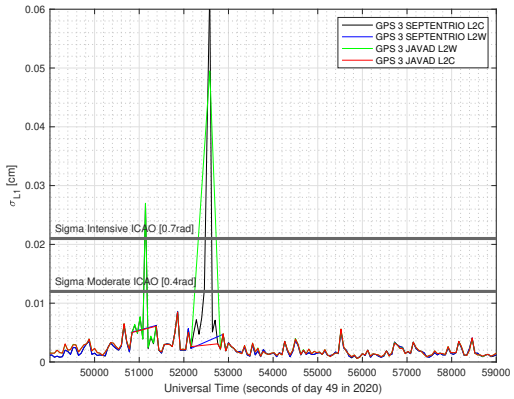

(a) All four GPS 3

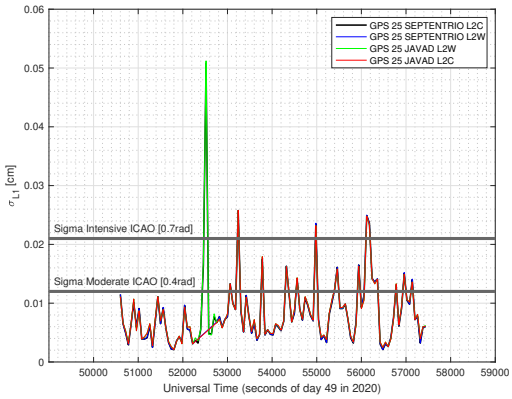

(b) All four GPS 25

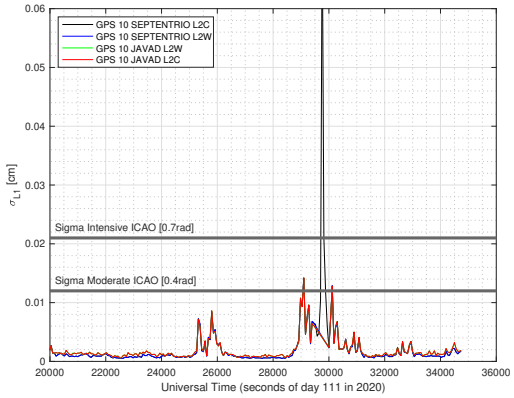

(c) All four GPS 10

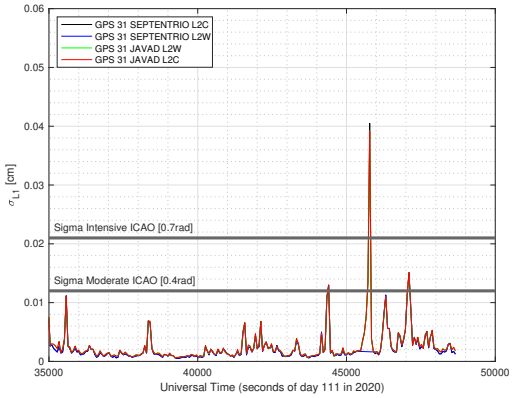

(d) All four GPS 31

Figure 6.5: All four GPS Plots

Since the signal in L1, all the results should be identical since, in this case, L2 does not intervene in the formation of the L1 signal. Thus, all the graphs should present the same level of scintillation for the same instant of time. This conclusion is altered by the fact of data gaps. There are periods of time in which the receiver is not able to follow the satellite tracking and a cycle-slip occurs. This idea is clearly depicted in Fig 6.2 where the GPS satellite 25 produces the same signal in the four graphs - regardless of which signal or receiver is used - except for those moments in which there is no data. It should be clarified that the detection of cycle slips is done using the two frequencies. That is why, even if it is L1, if there is a cycle-slip in L2, it is recorded at both frequencies.

This factor can produce that, for example in the case of GPS number 3 (Fig 6.1), the SEPTENTRIO receiver in use of L2C signal (Fig 6.1d) produces higher scintillation values than those registered by the JAVAD receiver in Fig 6.1a. In fact, the two are identical, the same signal is reproduced, the problem is that in the first case a cycle-slip occurs and the loss of data causes the value of σ_{L1} to be calculated with fewer points and therefore gives as a result a smaller value. In the case of day 111, satellite number 10 presents the same data in the four graphs (Fig 6.3) except for the scintillation peak where, depending on the receiver, there is data or a cycle-slip occurs.

If the emphasis is now on differences, starting with the case of GPS satellite number 3, it is found that the JAVAD receiver is able to follow the tracking of the signal when the scintillation peak occurs towards the 54000 (Fig 6.1a) using L2W but loses the signal and does not produce any data during the same period of time if the L2C signal is used for this (Fig 6.1c).

Continuing with the same GPS, it is clearly observed how in the case of using a SEPTENTRIO receiver does not register data during the scintillation peaks if L2W is used (Fig 6.1b) but instead, it does register even higher values of scintillation if the L2C signal is used (Fig 6.1d).

The behavior of the receivers is repeated for another satellite, in this case, number 25 and in another period of time in which a scintillation peak also occurs (Fig 6.2)

For the satellites of day 111, the situation is practically the same. GPS satellite number 10 produces a scintillation peak that is only able to track the SEPTENTRIO receiver using the L2C signal (Fig. 6.3d). For the JAVAD receiver, this peak is invisible and it is also invisible for SEPTENTRIO if it uses the L2W signal (Fig 6.3).

Finally, in the case of satellite 31, the scintillation peak occurs around 46000. This peak is seen by the JAVAD receiver (Fig 6.4), using any of the signals (L2W or L2C) but nevertheless, only the SEPTENTRIO receiver using L2C can follow the peak, since if receiver uses L2W it can be seen that there is no data for the period.

It could be concluded that the JAVAD receivers are more robust when using the L2W.

Instead, the SEPTENTRIO receiver is even more robust than the JAVAD if the L2C signal is used. The L2W signal of the SEPTENTRIO receiver is not capable of obtaining data in the seconds that a scintillation occurs. However, it should not be forgotten that it is really the same signal for each case and the only difference lies at moments in which a cycle-slip occurs due to the lack of data.

Fig. 6.5 summarizes the four plots seen by each satellite in a single plot in order to appreciate more easily the idea discussed in the two previous paragraphs.

6.2 $\sigma_{\phi L_{GF}}$ Analysis

Given the indications and the nature of the GF combination that, as Eq. 6.1, uses the L2 signal, different results may be obtained depending on which signal (L2C or L2W) and which receiver (JAVAD or SEPTENTRIO) is used to calculate the $\sigma_{\phi L_{GF}}$.It should be remembered that the L1 signal remains unchanged.

6.2.1 Results

Now, the analysis results for the geometry-free combination are shown for the same satellites and time intervals as the previous case in order to be able to compare. First, the results of GPS 3 and 25 of day 49 are presented and then the results of GPS 10 and 31 of day 111.

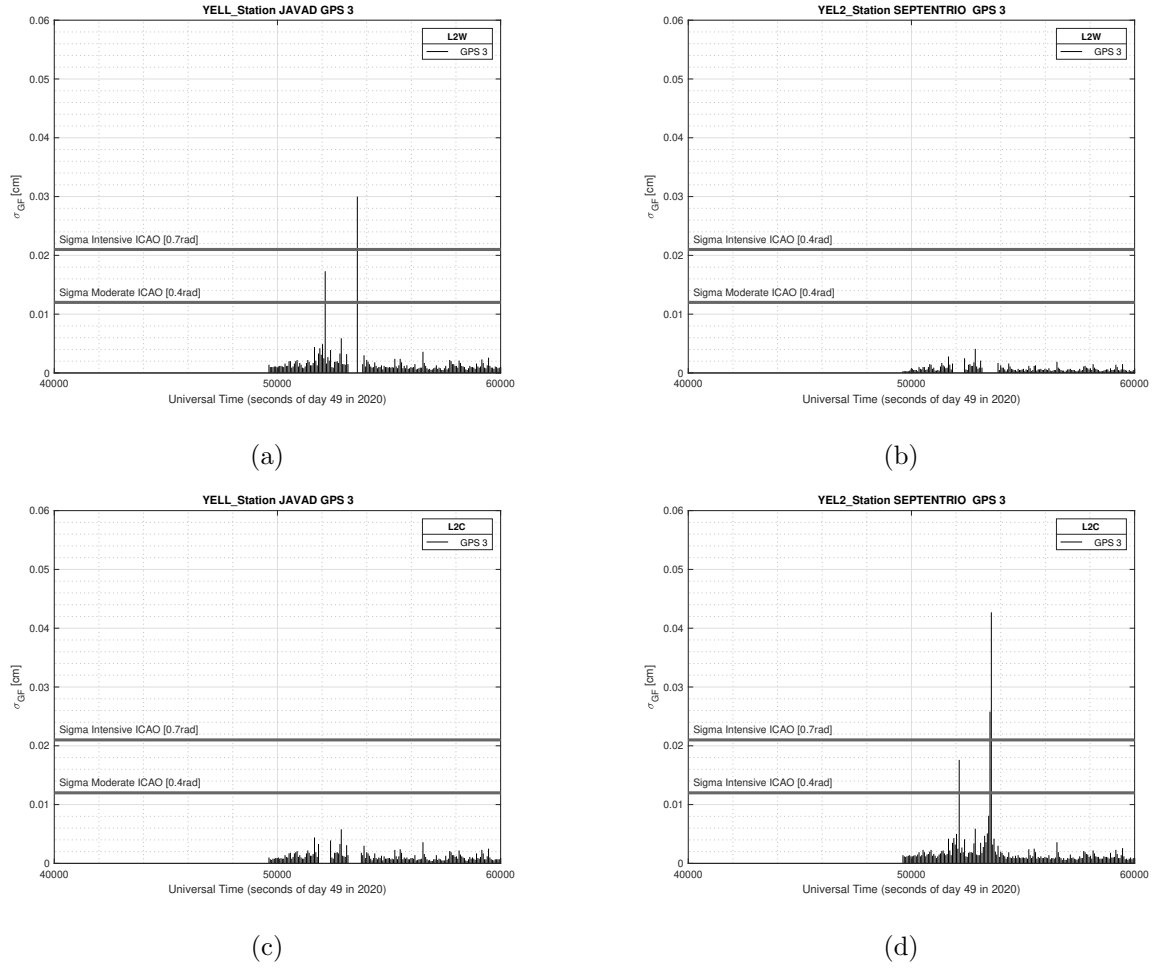

Figure 6.6: GPS 3 on 49th Day of 2020

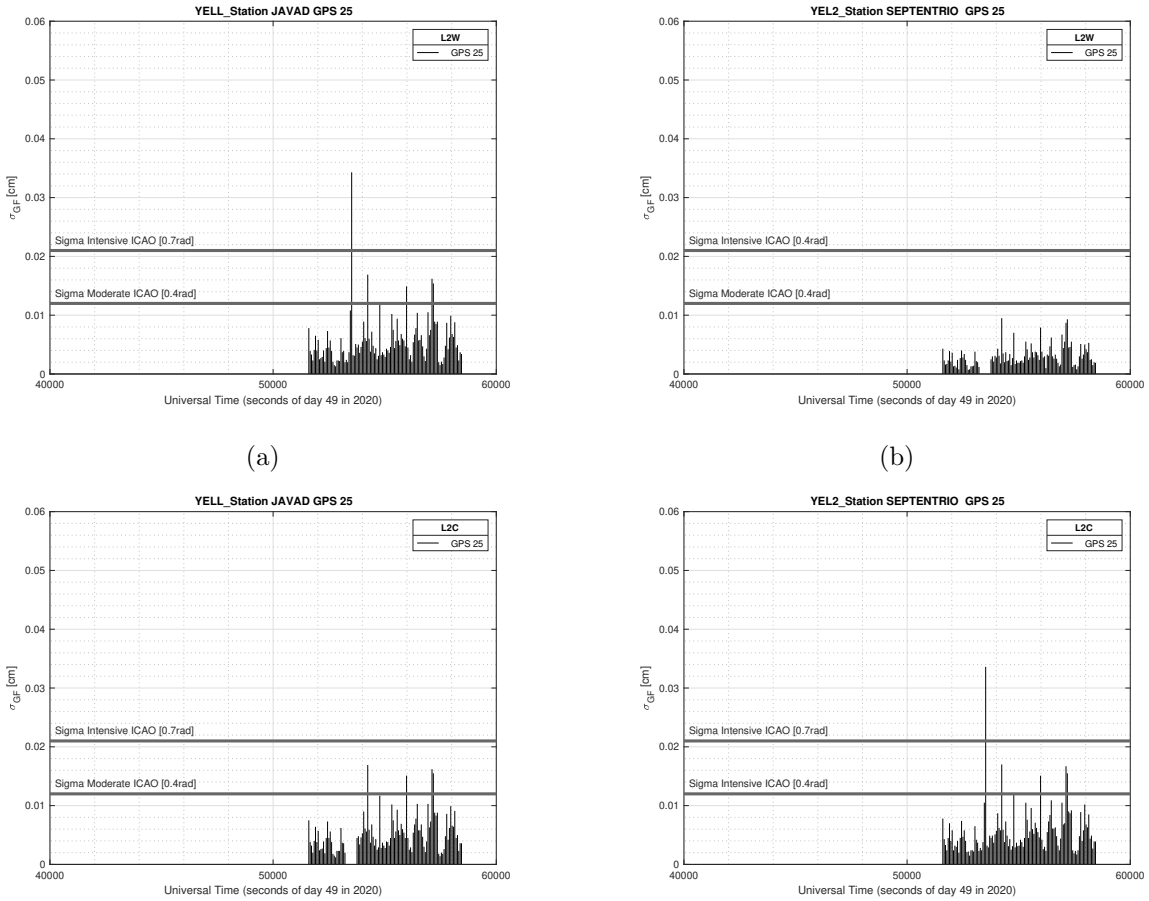

Figure 6.7: GPS 25 on 49th Day of 2020

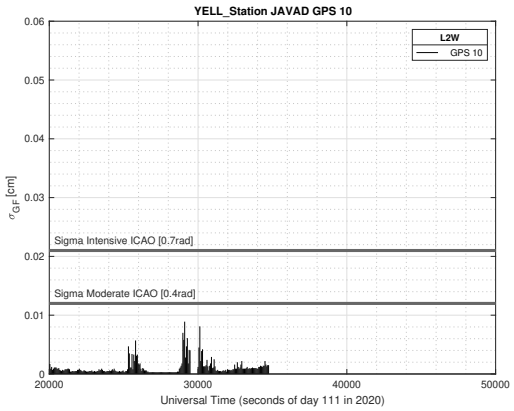

(a)

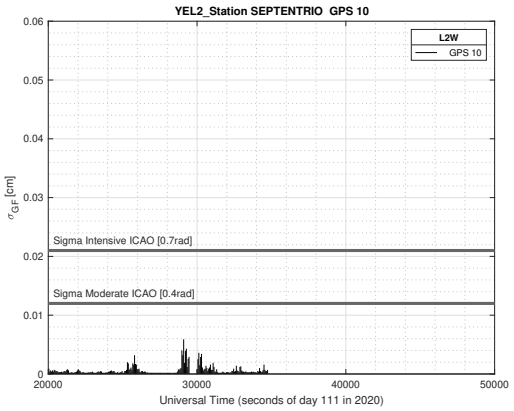

(b)

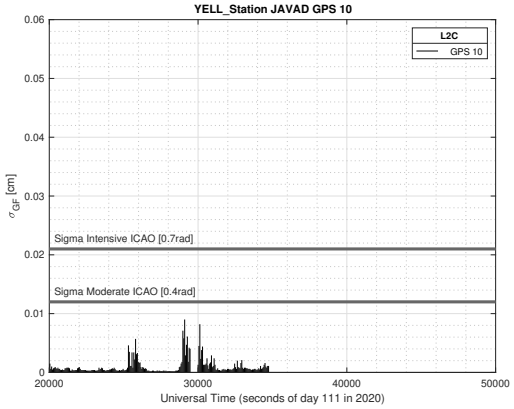

(c)

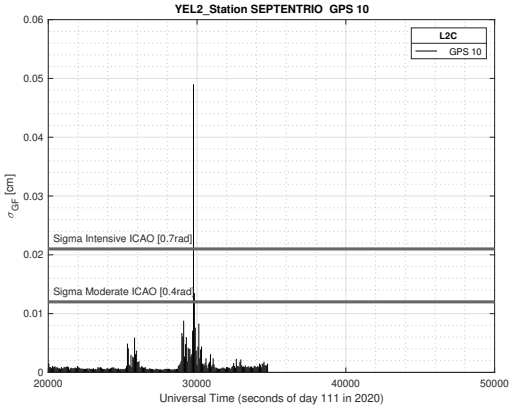

(d)

Figure 6.8: GPS 10 on 111th Day of 2020

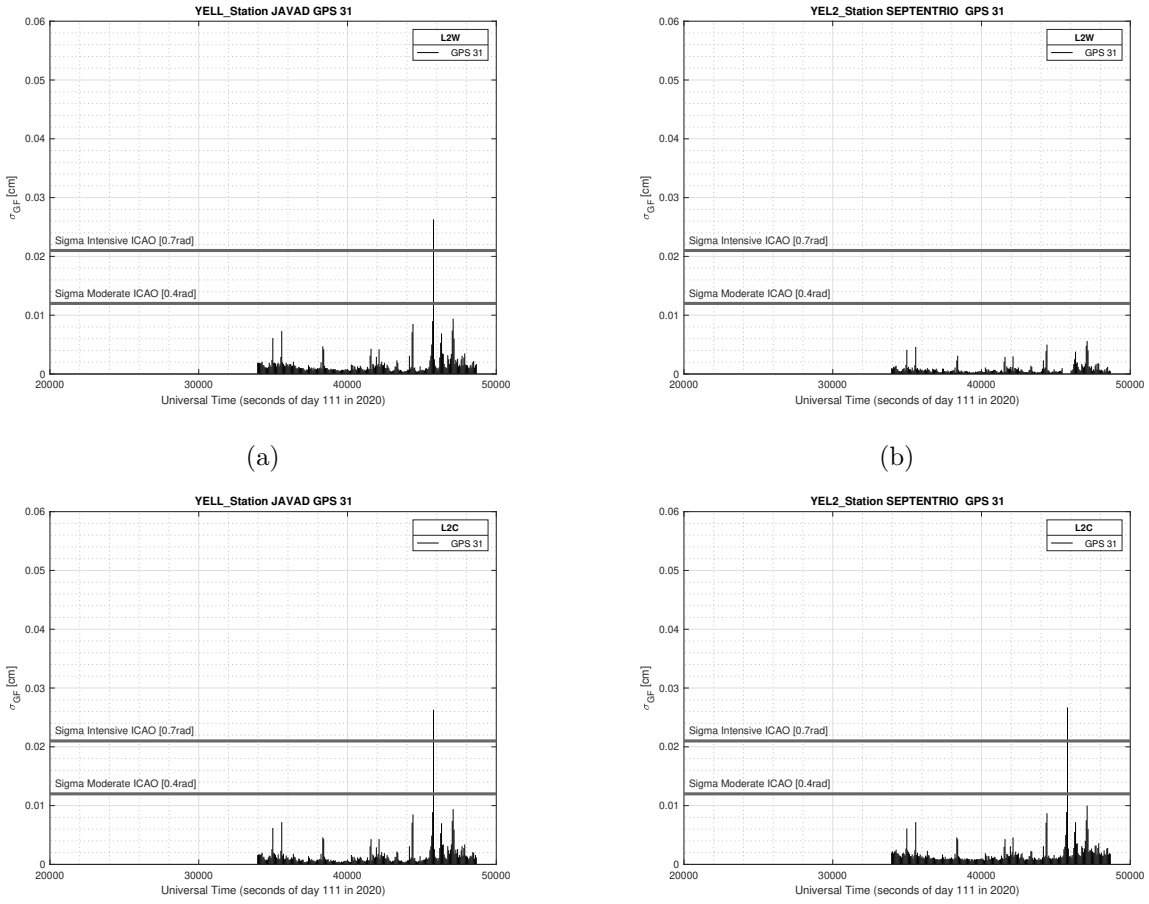

Figure 6.9: GPS 31 on 111th Day of 2020

As it can be seen, the problem that existed in the previous section in relation to the lack of data due to the cycle-slips that occur when the satellites lose tracking still happens. Therefore, everything discussed in the previous section applies to the results of Fig 6.6 to Fig 6.9. However, there is an added difference: If attention is focused on the figure (b) of each satellite, it can seen how the signal level is reduced by a tenths of a centimeter. For example, for the GPS 10 satellite, (Fig 6.8), the signal peaks seen around 30000 seconds reach almost 0.01 cm, except for Fig. 6.8b where they are far from reaching that level. The same happens in the case of GPS 31 where Fig. 6.9b does not exceed 0.005 cm at any time. It can be concluded that, in the case of SEPTENTRIO using L2W, a lower signal level on $\sigma_{\phi L_{GF}}$ (reduced scintillation effect) is obtained compared to the use of L2C or even of either of the two L2 signals in JAVAD receivers. This result is closely related to the GF combination that contains L2 which in turn is contaminated by L1 and the way in which L2W is generated.

In the following graphs that summarize the previous plots, it can be seen how the signal level of $\sigma_{\phi L_{GF}}$ SEPTENTRIO L2W (blue line) is below the other signals level. As it is mentioned before, data gaps are shown as straight lines.

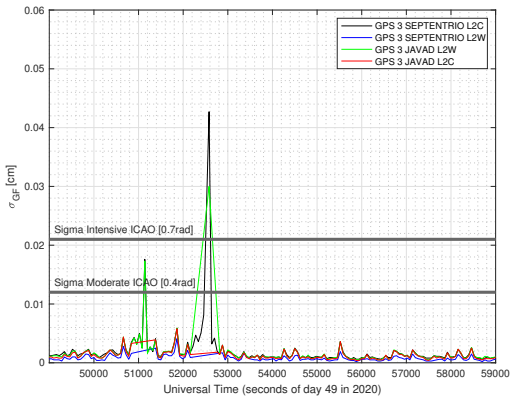

(a) All four GPS 3

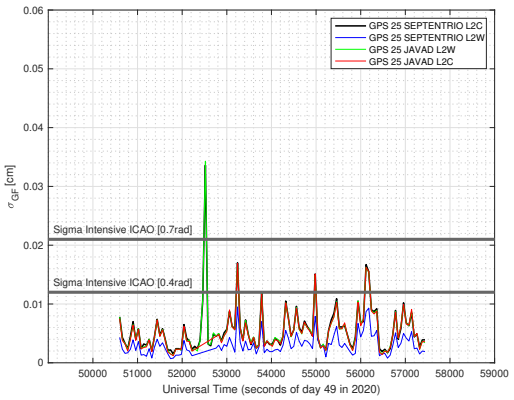

(b) All four GPS 25

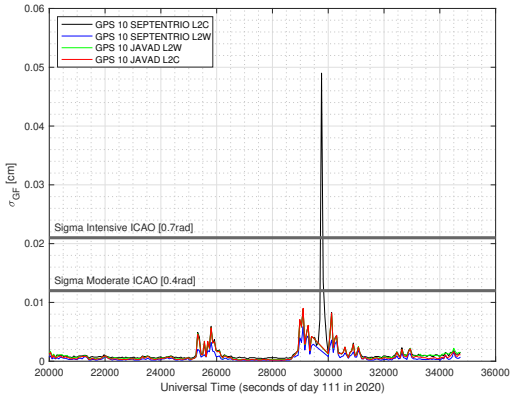

(c) All four GPS 10

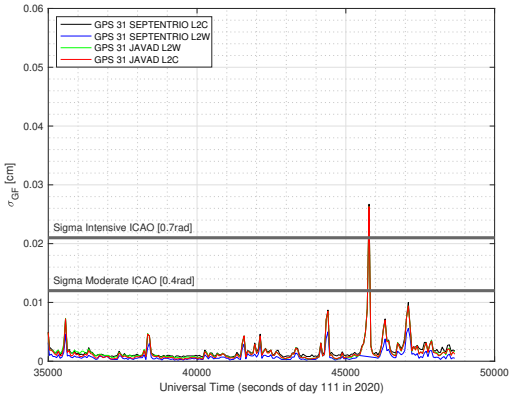

(d) All four GPS 31

Figure 6.10: All four for GF combination

6.3 $\sigma_{\phi L_{IF}}$ Analysis

This combination of signals represented by Eq.6.2 , is also affected by the use of L2W /L2C in SEPTENTRIO receivers, as in the previous case.

Now, the analysis results for the IF combination are shown for the same satellites and time intervals as the previous case in order to be able to compare. First, the results of GPS 3 and 25 of day 49 are presented and then the results of GPS 10 and 31 of day 111.

6.3.1 Results

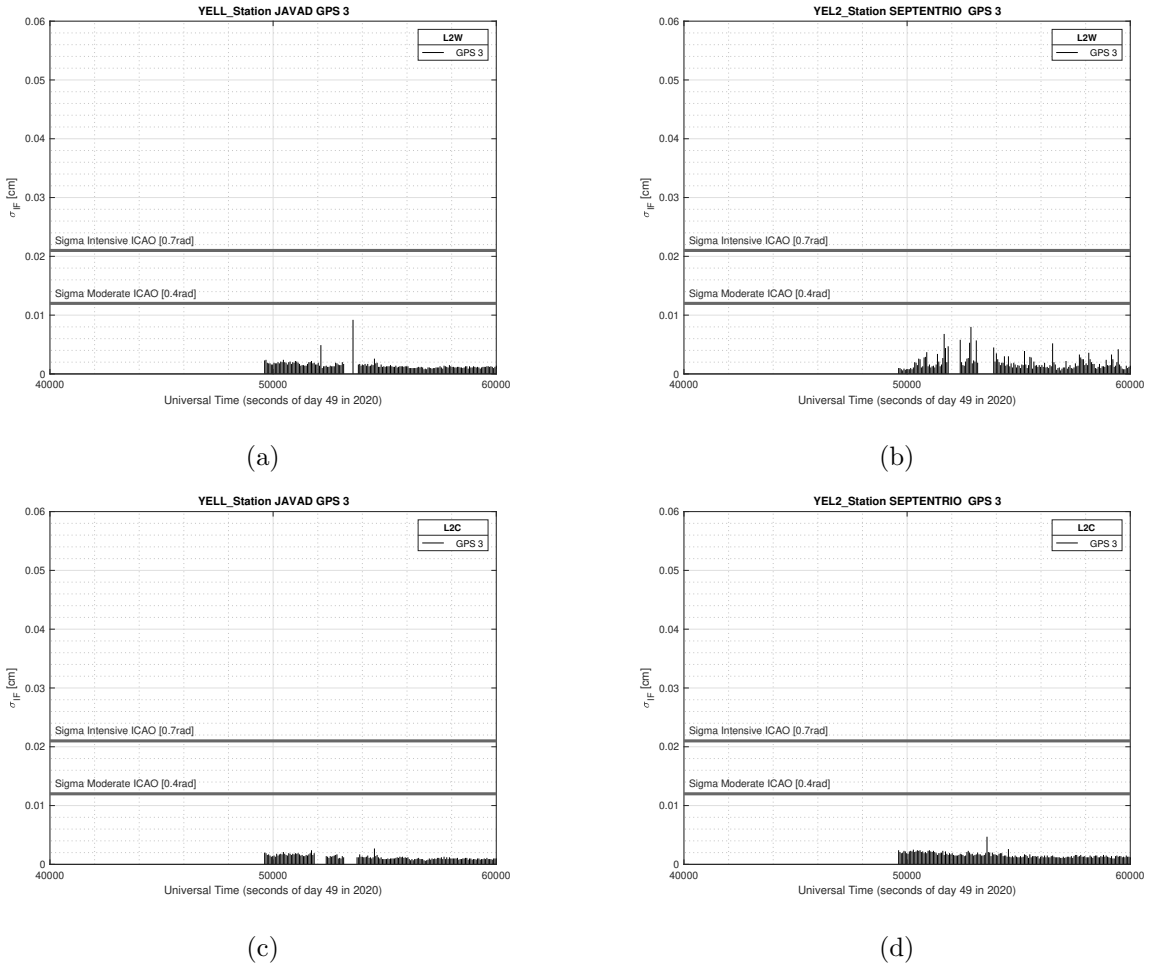

Figure 6.11: GPS 3 on 49th Day of 2020

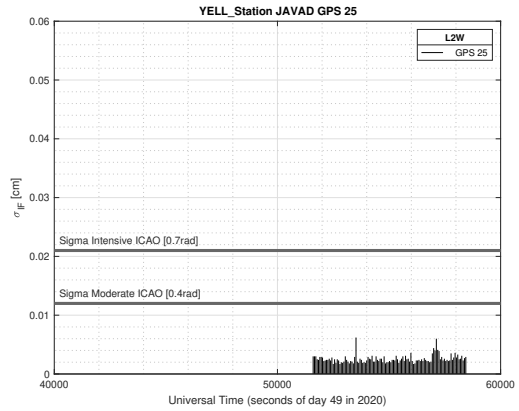

(a)

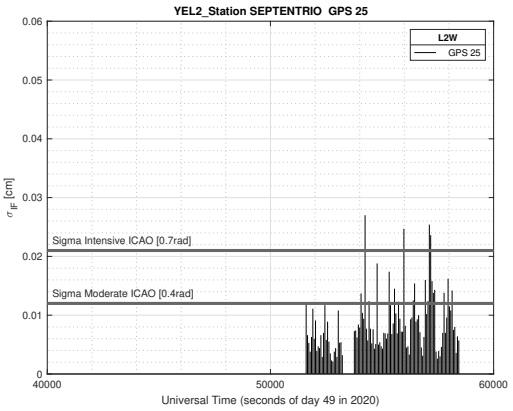

(b)

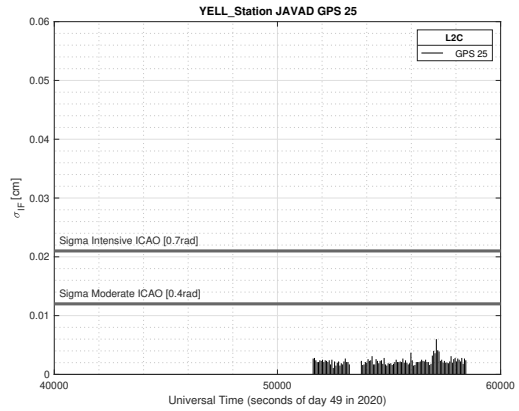

(c)

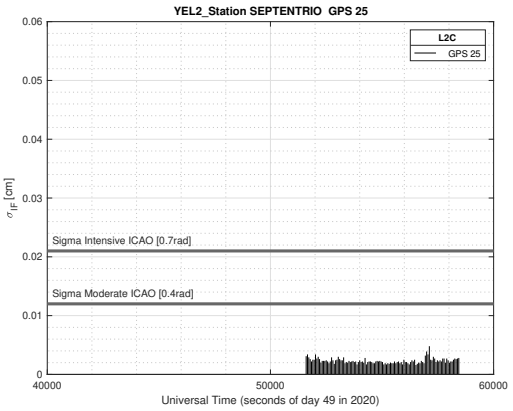

(d)

Figure 6.12: GPS 25 on 49th Day of 2020

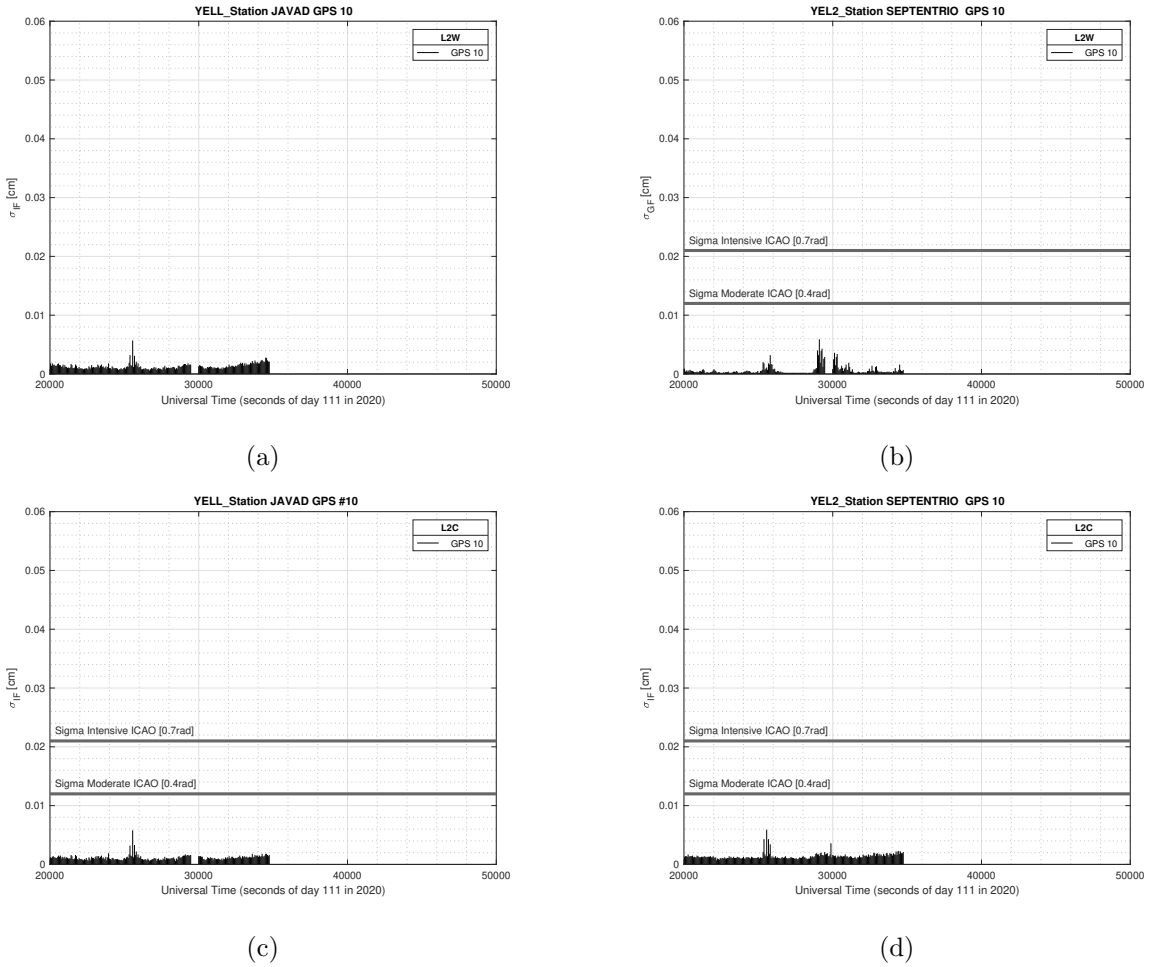

Figure 6.13: GPS 10 on 111th Day of 2020

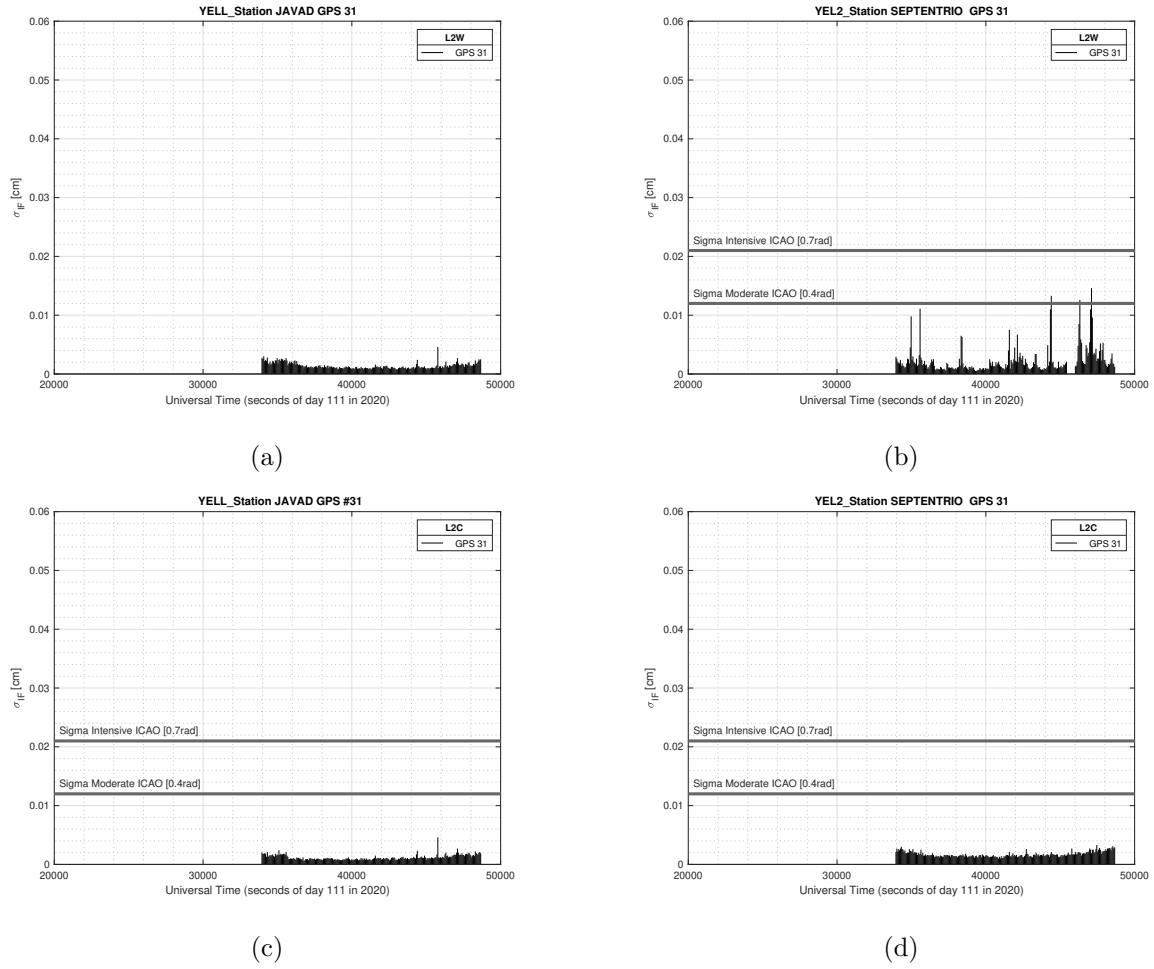

Figure 6.14: GPS 31 on 111th Day of 2020

However, it can be seen that the opposite case occurs, that is, the $\sigma_{\phi L_{IF}}$ signal level of the graphs (b) in each satellite is slightly higher (more noisy) than the others. A clear example is Fig 6.12 b where the samples are much noisy, exceeding the scintillation thresholds. Therefore, as a conclusion, it can be observed that the use of L2W in SEPTENTRIO receivers causes a much noisier signal than if L2C is used. This fact is especially critical for two reasons; first, it should be remembered that the IF combination is used for precise navigation. Therefore, the more noise in signal results the less positioning, with more errors. Later, the GPS of the IIR blocks only have the L2W signal option so they cannot use L2C to avoid it.

In the following graphs that summarize the previous plots, it can be seen how the signal level of $\sigma_{\phi L_{IF}}$ SEPTENTRIO L2W (blue line) is above the other signals level. In addition, all remaining colors have similar levels. As it is mentioned before, data gaps are shown as straight lines.

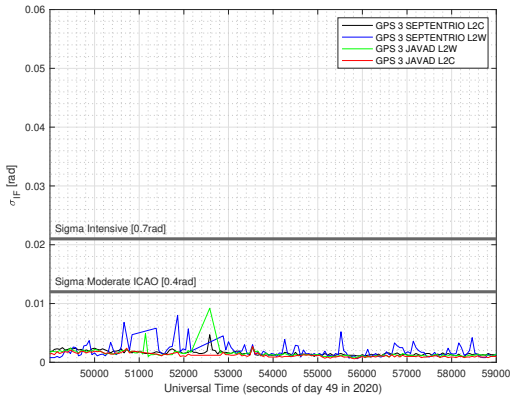

(a) All four GPS 3

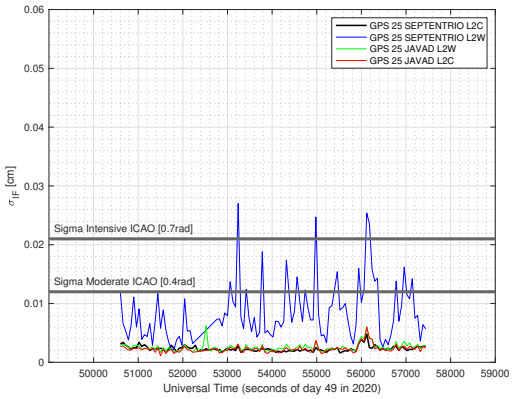

(b) All four GPS 25

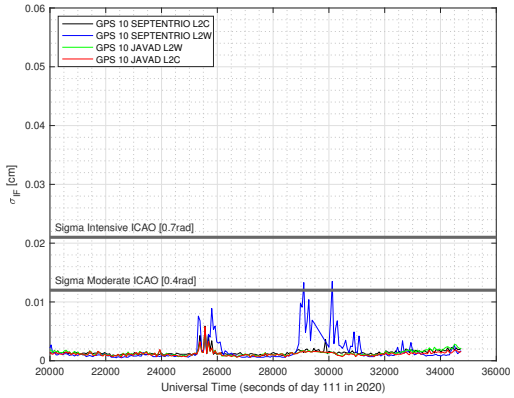

(c) All four GPS 10

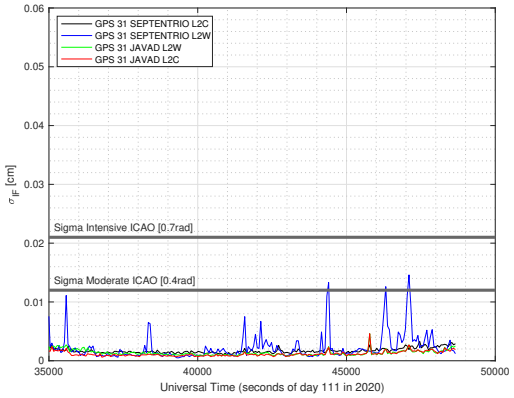

(d) All four GPS 31

Figure 6.15: All four for IF combination

Chapter 7

Conclusions

This chapter aims to highlight the most relevant conclusions obtained in the cours of the TFM. That is why the most relevant information will be summarized in order to highlight, clarify and conjecture the most important aspects obtained in this study on scintillation.

In a first instance, when analyzing the scintillation along the days of 2020 in Chapter 5, it carried out focussing on two variables: Amplitude Scintillation incidence S_4 and Phase Scintillation incidence $\sigma\phi$. However, it has been possible to demonstrate thanks to the results obtained that S_4 does not conclude since it is not possible to distinguish those days with more scintillation from those with almost no scintillation. In contrast, with its highest treshold, *Sigma Intensive*, it shows how clearly the scintillation is detected in the stations with a high latitude. That is why from that moment on, the study continues having the second variable analyzed.

Another conclusion drawn in the same chapter is the difference between the scintillation data according to the constellation observed. It has been seen how, in the case of GLONASS, the results presented a range of warm colors that did not mean that there was more scintillation, they were simply sequels of noise due to clocks and the satellite. For this reason, the result of all the constellations, was contaminated by this particular case. That is why, it can be concluded that GLONASS constellation data cannot be used as a robust scintillation indicator when GD is used, due to inherent noise.

On the opposite side, there are Galileo results that are low values and thus, Galileo data can clearly identify days with scintillation episodes. This is consistent with the more stable oscillators onboard the Galileo satellites that produce measurements with a reduced level of noise.

However, the most interesting case occurred in the GPS constellation where the results of the stations and days involving the L2W signal present higher noise depending on how the receiver calculates the GPS signal differently. That is why the next chapters have focused on the study

of this constellation.

In Chapter 5, when analyzing the GPS satellites of the two days with the most scintillation in different receivers (JAVAD or SEPTENTRIO), two important conclusions should be highlighted. First, the base noise of the SEPTENTRIO receiver when there is no scintillation is lower than the base noise presented by JAVAD receivers. Second, it was observed that the SEPTENTRIO receiver, using the L2C signal, is able to record higher scintillation values of GPS signals that are lower or non-existent in the JAVAD receiver. This last is especially important in the study the behavior of the ionosphere, where SEPTENTRIO receiver with the L2C signal has to be chosen because it does not produce a data gap and is capable of capturing the highest scintillation data.

Chapter 6 - focused on two stations, certain satellites and instants - present a very relevant conclusion: the use of L2W in SEPTENTRIO causes a much noisier signal of the IF combination (the one which is used to navigate) than if L2C is used. Therefore, if you have to navigate and PPP is required, you need a satellite of a block that already contains the L2C signal. Otherwise, navigation will be affected by scintillation. In addition, the use of L2W in SEPTENTRIO also causes a low aignal values of the GF combinationa, so the ionospheric remote sensing community would be affected.

Chapter 8

Budget

This project has been carried out remotely thanks to the contribution of the gAGE group of access to a virtual machine where the necessary data stored. Therefore, the budget summary would be the hours invested in the project. For a price of 12 euros per hour and about 400 hours dedicated both to reading and searching for information and generating results and their conclusions, the final price is 4800 euros.

In addition, if a PC has an average consumption of 0.14 euros/kWh and for this project it is needed a PC and a server, the total price for electricity is $2\times$ 0.14 euros/kWh $\times 400h = 112$ euros.

Chapter 9

Analysis and assessment of the environmental and social implications

Despite being a technical project, it has direct implications for society. The improvement of the positioning in scintillation conditions will improve in the logistics sector (i.e, more precise and direct routes), in air and maritime navigation (ie, improvements in routes and trajectories as well). In turn, this fact reduces fuel consumption and therefore CO_2 emissions into the atmosphere.

Bibliography

[1] B. Briggs and I. Parkin, "On the variation of radio star and satellite scintillations with zenith angle," *Journal of Atmospheric and Terrestrial Physics*, vol. 25, no. 6, pp. 339–366, 1963.

[2] F. S. Crawford, "Berkeley physics course," 1968.

[3] D. Wells, N. Beck, A. Kleusberg, E. J. Krakiwsky, G. Lachapelle, R. B. Langley, K.-p. Schwarz, J. M. Tranquilla, P. Vanicek, and D. Delikaraoglou, "Guide to GPS positioning," in *Canadian* GPS *Assoc*, Citeseer, 1987.

[4] J. Aarons, "50 years of radio-scintillation observations," *IEEE Antennas and Propagation Magazine*, vol. 39, no. 6, pp. 7–12, 1997.

[5] X. Pi, A. Mannucci, U. Lindqwister, and C. Ho, "Monitoring of global ionospheric irregularities using the worldwide GPS network," *Geophysical Research Letters*, vol. 24, no. 18, pp. 2283–2286, 1997.

[6] J. Zumberge, M. Heflin, D. Jefferson, M. Watkins, and F. Webb, "Precise point positioning for the efficient and robust analysis of GPS data from large networks," *Journal of geophysical research: solid earth*, vol. 102, no. B3, pp. 5005–5017, 1997.

[7] I. W. Selesnick and C. S. Burrus, "Generalized digital butterworth filter design," *IEEE Transactions on signal processing*, vol. 46, no. 6, pp. 1688–1694, 1998.

[8] K. Woo, "Optimum semi-codeless carrier phase tracking of l2," in *Proceedings of the 12th International Technical Meeting of the Satellite Division of The Institute of Navigation (ION* GPS *1999)*, 1999, pp. 289–306.

[9] B. Forte, "Optimum detrending of raw GPS data for scintillation measurements at auroral latitudes," *Journal of atmospheric and solar-terrestrial physics*, vol. 67, no. 12, pp. 1100–1109, 2005.

[10] J. S. Subirana, J. J. Zornoza, and M. Hernández-Pajares, "GNSS data processing. volume 1: Fundamentals and algorithms," *ESA Communications ESTEC, PO Box*, vol. 299, p. 2200, 2013.

[11] European GNSS Agency, "GNSS market report issue 5," 2017.

[12] J. Juan, A. Aragon-Angel, J. Sanz, G. González-Casado, and A. Rovira-Garcia, "A method for scintillation characterization using geodetic receivers operating at 1 hz," *Journal of Geodesy*, vol. 91, no. 11, pp. 1383–1397, 2017.

[13] X. Pi, B. A. Iijima, and W. Lu, "Effects of ionospheric scintillation on GNSS-based positioning," *NAVIGATION, Journal of the Institute of Navigation*, vol. 64, no. 1, pp. 3–22, 2017.

[14] Z. Yang and Z. Liu, "Investigating the inconsistency of ionospheric roti indices derived from GPS modernized l2c and legacy l2 p (y) signals at low-latitude regions," *GPS solutions*, vol. 21, no. 2, pp. 783–796, 2017.

[15] J. M. Juan, J. Sanz, A. Rovira-Garcia, G. González-Casado, D. Ibáñez, and R. O. Perez, "Aatr an ionospheric activity indicator specifically based on gnss measurements," *Journal of Space Weather and Space Climate*, vol. 8, A14, 2018.

[16] A. M. McCaffrey, P. Jayachandran, R. B. Langley, and J.-M. Sleewaegen, "On the accuracy of the gps l2 observable for ionospheric monitoring," *GPS Solutions*, vol. 22, no. 1, pp. 1–7, 2018.

[17] International Civil Aviation Organization, *Doc 10100 - Manual on Space Weather Information in Support of International Air Navigation*. INTERNATIONAL CIVIL AVIATION ORGANIZATION, 2019, ISBN: 978-92-9258-662-1.

[18] V. K. Nguyen, A. Rovira-Garcia, J. M. Juan, J. Sanz, G. González-Casado, T. H. Ta, *et al.*, "Measuring phase scintillation at different frequencies with conventional GNSS receivers operating at 1 hz," *Journal of Geodesy*, vol. 93, no. 10, pp. 1985–2001, 2019.

[19] A. Rovira Garcia, J. M. Juan Zornoza, J. Sanz Subirana, G. González Casado, and M. Escudero Royo, "The navscin project: Towards high-accuracy navigation under scintillation," in *Proceedings FIG Working Week 2019: 22-26 April 2019 Hanoi, Vietnam*, 2019, pp. 1–10.

[20] GSA, GNSS *User Technology Report*. Luxembourg: Publications Office of the European Union, 2020, 2020, ISBN: 978-92-9206-049-7.

[21] A. Rovira-Garcia, G. González-Casado, J. M. Juan, J. Sanz, and R. O. Pérez, "Climatology of high and low latitude scintillation in the last solar cycle by means of the geodetic detrending technique," in *Proceedings of the 2020 International Technical Meeting of The Institute of Navigation*, 2020, pp. 920–933.

[22] ESA, GPS *signal plan - navipedia*. [Online]. Available: `https://gssc.esa.int/navipedia/index.php/GPS_Signal_Plan`, (accessed: 09.05.2021).

[23] U. D. of Homeland Security, GPS *constellation status*. [Online]. Available: `https://www.navcen.uscg.gov/?Do=constellationStatus`, (accessed: 09.05.2021).